9

Scattered-light DOAS Measurements

The absorption spectroscopic analysis of sunlight scattered by air molecules and particles as a tool for probing the atmospheric composition has a long tradition. Götz et al. (1934) introduced the 'Umkehr' technique, which is based on the observation of a few select wavelengths of scattered sunlight. The analysis of strong absorption in the ultraviolet allowed the retrieval of ozone concentrations in several atmospheric layers, which yielded the first remotely measured vertical profiles of (stratospheric) ozone. The COSPEC technique developed in late 1960s was the first attempt to study tropospheric species by analysing scattered sunlight in a wider spectral range with the help of an optomechanical correlator (Millan et al. 1969; Davies 1970), see Sect. 5.7. It has been applied over three decades for measurements of total emissions of SO_2 and NO_2 from various sources, e.g. industrial emissions (Hoff and Millan, 1981) and volcanic plumes (Stoiber and Jepsen, 1973; Hoff et al. 1992). Scattered sunlight was also used to study stratospheric and tropospheric NO_2, as well as other stratospheric species by ground-based differential optical absorption spectroscopy (DOAS) (Noxon, 1975; Noxon et al., 1979; Pommereau, 1982; McKenzie et al., 1982; Solomon et al., 1987). An overview of different scattered light techniques is given in Table 9.1.

Scattered sunlight DOAS is an experimentally simple and very effective technique for the measurement of atmospheric trace gases and aerosols. Since scattered light DOAS instruments analyse radiation from the sun, rather than relying on artificial sources, they are categorised as **passive** DOAS instruments (see also Chap. 6).

All passive DOAS instruments are similar in their optical setup, which essentially consists of a telescope to collect light, coupled to a spectrometer–detector combination (see Chap. 7). However, different types of passive DOAS instruments employ a wide variety of observation geometries for different platforms and measurement objectives.

The earliest scattered light DOAS applications were ground-based and predominately observed light from the zenith (Noxon, 1975; Syed and Harrison, 1980; McMahon and Simmons, 1980; Pommereau, 1982, 1994;

U. Platt and J. Stutz, *Scattered-light DOAS Measurements.* In: U. Platt and J. Stutz,
Differential Optical Absorption Spectroscopy, Physics of Earth and Space Environments,
pp. 329–377 (2008)
DOI 10.1007/978-3-540-75776-4_9

Table 9.1. Overview and history of the different scattered light passive DOAS applications

Method	Measured quantity	No. of axes, technique	References
COSPEC	NO_2, SO_2, I_2	1, (S)	Millan et al., 1969; Davies, 1970; Hoff and Millan, 1981; Stoiber and Jepsen, 1973; Hoff et al., 1992
Zenith scattered light DOAS	Stratospheric NO_2, O_3, OClO, BrO, IO	1	Noxon, 1975; Noxon et al., 1979; Harrison, 1979; McKenzie and Johnston, 1982; Solomon et al., 1987a; Solomon et al., 1987b, McKenzie et al., 1991; Fiedler et al., 1993; Pommereau and Piquard, 1994a,b; Kreher et al., 1997; Wittrock et al., 2000a
Zenith sky + Off-axis DOAS	Stratospheric OClO	2	Sanders et al., 1993
Off-axis DOAS	Stratospheric BrO profile	1	Arpaq et al., 1994
Zenith scattered light DOAS	Tropospheric IO, BrO	1	Friess et al., 2001, 2004
Off-axis DOAS	Tropospheric BrO	1	Miller et al., 1997
Sunrise Off-axis DOAS + direct moonlight	NO_3 profiles	2, S	Weaver et al., 1996; Smith and Solomon, 1990; Smith et al., 1993
Sunrise Off-axis DOAS	Tropospheric NO_3 profiles	1	Kaiser, 1997; von Friedeburg et al., 2002
Aircraft-DOAS	Tropospheric BrO	2	McElroy et al., 1999
Aircraft zenith sky + Off-axis DOAS	“near in-situ” Stratospheric O_3	3	Petritoli et al., 2002
AMAX-DOAS	Trace gas profiles	8+, M	Wagner et al., 2002; Wang et al., 2003; Heue et al., 2003
Multi Axis DOAS	Tropospheric BrO profiles	4, S	Hönninger and Platt, 2002
Multi Axis DOAS	Tropospheric BrO profiles	4, S	Hönninger et al., 2003b

Table 9.1. (continued)

Multi Axis DOAS	Trace gas profiles	2-4, M	Löwe et al., 2002; Oetjen, 2002; Heckel, 2003
Multi Axis DOAS	NO_2 plume	8, M	V. Friedeburg, 2003
Multi Axis DOAS	BrO in the marine boundary layer	6, S/M	Leser et al., 2003; Bossmeyer, 2002
Multi Axis DOAS	BrO and SO_2 fluxes from volcanoes	10, S	Bobrowski et al., 2003
Multi Axis DOAS	BrO emissions from a Salt Lake	4, S	Hönninger et al., 2003a
Multi Axis DOAS	IO emissions from a Salt Lake	6, S	Zingler et al., 2005

S = Scanning instrument, M = Multiple telescopes.

McKenzie et al., 1982, 1991; Solomon et al., 1987, 1988, 1993; Perner et al., 1994; Van Roozendael et al., 1994; Slusser et al., 1996). This Zenith Scattered Light–DOAS (ZSL-DOAS) geometry is particularly useful for the observation of stratospheric trace gases, and has made major contributions to the understanding of the chemistry of stratospheric ozone, in particular through the measurement of stratospheric NO_2, OClO, BrO, and O_3 (Pommereau, 1982, 1994; McKenzie et al., 1982, 1991; Solomon et al., 1987, 1988, 1993; Perner et al., 1994; Van Roozendael et al., 1994a,b,c; Slusser et al., 1996; Sanders, 1996; Sanders et al., 1997).

The next development in scattered light DOAS employed an off-axis geometry (Sanders et al., 1993) and observed the sky at one low-elevation angle to improve the sensitivity of the instrument. Recently, this idea was expanded by employing multiple viewing geometries. This Multi-Axis DOAS (MAX-DOAS) method typically employs 3–10 different viewing elevations (Winterrath et al., 1999; Friess et al., 2001; Hönniger and Platt, 2003; Wagner et al., 2004). In contrast to the earlier instruments, MAX-DOAS is more sensitive to tropospheric trace gases, and thus offers a large number of possible applications. It should be noted that at the time of writing this book, MAX-DOAS was still very much a method in development, and many of the possible applications have not been extensively explored. The most recent ground-based passive DOAS application makes use of modern solid-state array detectors, expanding the number of viewing channels to hundreds. This imaging DOAS can provide a spectroscopic 'photo' of the composition of the atmosphere, e.g. of the emissions from a smoke stack.

Early on in the development and use of scattered light DOAS, platforms other than the ground were explored. Schiller et al. (1990) report ZSL-DOAS measurements on-board the NASA DC8 research aircraft. Similar measurements were reported by McElroy et al. (1999) and Pfeilsticker and Platt

(1994). The use of scattered light DOAS on mobile platforms allows the access to remote areas that can only be reached through air, e.g. the remote ocean and polar regions. In the recent years, MAX-DOAS has also been adapted to airborne platforms. While ground-based MAX-DOAS typically uses viewing elevations from the zenith to the very low elevations, the range of airborne MAX-DOAS extends from zenith viewing to nadir (downwards) viewing, thus covering a whole 180°. This viewing direction arrangement allows the measurement of trace gases below and above the aircraft (Wang et al., 2003).

One of the most exciting developments of passive DOAS in the last decade was the launch of various spaceborne DOAS instruments (see Chap. 11). The instruments typically operate in a nadir viewing mode to provide global coverage of the distribution of trace gases such as NO_2 and HCHO. Instruments such as SCHIAMACHY allow the limb-observations of scattered sunlight, with the goal of deriving vertical trace gas profiles.

A common characteristic, that distinguishes scattered light absorption spectroscopy measurements from active DOAS (for examples see Chap. 10) or direct sunlight DOAS is the lack of a clearly defined light path. Considerable effort thus has to be invested in converting the observed trace gas absorption strength to a quantity that is useful for the interpretation of observations. This usually involves modelling the radiation transport in the atmosphere (see Chap. 3) to determine an effective light path length in the atmosphere.

This chapter provides a general introduction into the methods required to interpret scattered light DOAS measurements. We will begin by introducing the basic concepts that are needed to understand scattered light DOAS, and then discuss the details of radiative transfer calculations. Since the techniques to analyse the absorption spectra were already discussed in Chap. 8, we will concentrate on the interpretation of trace gas abundances prevailing along the atmospheric light path.

9.1 Air Mass Factors (AMF)

The classical concept of absorption spectroscopy as an analytical method is based on the knowledge of absorption path length and the assumption that the conditions along the light do not vary (Chap. 6). For scattered and direct sunlight DOAS measurements, in which the light crosses the vertical extent of the atmosphere, this assumption is usually not valid. New concepts thus have to be introduced to interpret these measurements. In this section we will introduce these concepts and the quantities that are necessary to quantitatively analyse DOAS observations. We will use an approach that loosely follows the history and development of the interpretation of spectroscopy observations beginning with direct sun observations, followed by zenith and off-axis scattered sunlight applications.

Before discussing the individual aspects of these observational strategies, it is useful to introduce the quantity that is commonly the final result of passive DOAS observations, the vertical column density (VCD). Historically, the vertical column density (V) has been defined as the concentration of a trace gas vertically integrated over the entire extent of the atmosphere:

$$V = \int_0^\infty c(z)\,dz\,. \tag{9.1}$$

In recent years, this concept has been expanded by varying the limits of integration to cover the stratosphere, troposphere, or height intervals of the atmosphere. We will, therefore, expand this equation by introducing partial columns:

$$V(z_1, z_2) = \int_{z_1}^{z_2} c(z)\,dz\,. \tag{9.2}$$

9.1.1 Direct Light AMF

The earliest applications of absorption spectroscopy in the atmosphere relied on the measurement of direct sun or moonlight. As a consequence of the movement of the solar or lunar disk in the sky (Fig. 9.1), the path length used in Lambert–Beer's law to convert the observed trace gas absorption changes as a function of the solar or lunar position. It is common to use the angle between the zenith and the sun or moon to quantify this position. This Solar (or Lunar)-Zenith-Angle (SZA, LZA), ϑ, is 0° when the sun or moon is in the zenith, and 90° when they are on the horizon. In addition, the Solar (Lunar)-Azimuth-Angle (SAZ, LAZ) is used to define the horizontal position. The SAZ (LAZ) is zero by definition when the sun or moon is in northern direction and increases clockwise. We can, however, see that the azimuth angle does not play an important role when interpreting direct solar or lunar measurements.

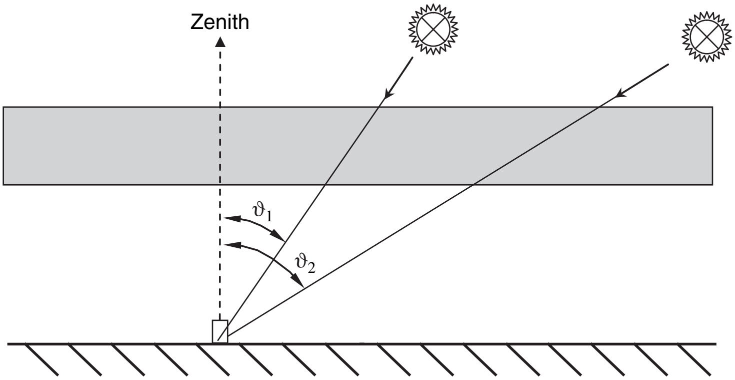

Fig. 9.1. Sketch of direct light observation geometries. In first approximation, the light path through a trace gas layer varies with $1/\cos\vartheta$ (ϑ = zenith angle of celestial body observed)

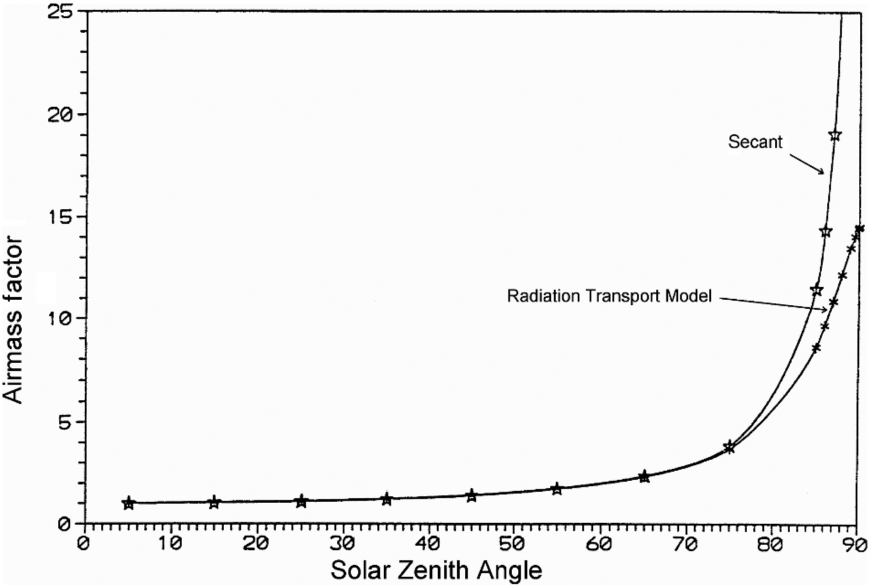

Fig. 9.2. Direct light air mass factors. Model calculations including curvature of earth as well as refraction inside the atmosphere are compared to the simple secants $\vartheta = 1/\cos\vartheta$ approximation. Deviations become apparent at $\vartheta > 70°$ (from Frank, 1991)

To describe the observations of trace gases, we introduce the 'slant column density' (SCD), S. Historically, SCD has been defined by the concentration integrated over the light path in the atmosphere.

$$S = \int_0^\infty c\,(s)\,ds\ . \tag{9.3}$$

In contrast to the definition of VCD in (9.1), the element of path ds does not need to be vertical. In the case sketched in Fig. 9.1, the SCD can be determined by the geometrical enhancement of slanted light path in the atmosphere, i.e. $ds = 1/\cos\vartheta\,dz$ for small SZA. This concept of the SCD will, however, lead to problems in the interpretation of scattered light observations, since the column seen by the instrument is an 'apparent' column, which is intensity weighted over an infinite number of different light paths through the atmosphere. We will, therefore, define SCD more generally from the observed column density as the ratio of measured differential optical density D' and known differential absorption cross-sections σ', i.e. $S = D'/\sigma'$ (see Chaps. 6 and 8).

To relate the observed SCD to the desired result of the measurement, i.e. the vertical column density, we now introduce the airmass factor (AMF), A, as:

$$A = \frac{S}{V}\ . \tag{9.4}$$

The AMF is the proportionality factor between the observed column density and the VCD (see Noxon et al., 1979). The most basic example of an AMF is the direct light AMF for an observation geometry where the instrument looks directly towards a celestial body (e.g. sun, moon, star), which is assumed to be point-like. Neglecting the curvature of earth and refraction in the atmosphere (i.e. for sufficiently small zenith angles), we obtain for the AMF as A_D (Fig. 9.1):

$$A_D = \frac{\text{length of slant path}}{\text{length of vertical path}} \approx \frac{1}{\cos\vartheta}\ . \tag{9.5}$$

Up to an SZA of ≈75°, (9.5) is a good approximation for the direct AMF (Fig. 9.2). Above 75°, effects such as the earth's curvature and atmospheric refraction have to be considered. Refraction in the atmosphere is caused by the dependence of the refractive index of air on temperature, pressure and thus its change with altitude.

9.1.2 Scattered Zenith Light AMF

A multitude of passive DOAS applications use scattered sunlight to measure trace gas absorptions. The telescopes in these scattered sunlight DOAS instruments are aimed at a point in the sky other than the sun or moon. Consequently, we need to consider the viewing direction of the DOAS telescope in addition to the solar position. This viewing direction is again characterised by two angles: the elevation, which gives the angle in the vertical between the horizon (for ground based instruments) and the viewing direction. The zenith in this case is at an elevation of $\alpha = 90°$. For downward-looking geometries, such as from airborne or satellite instruments, we will use negative values, i.e.

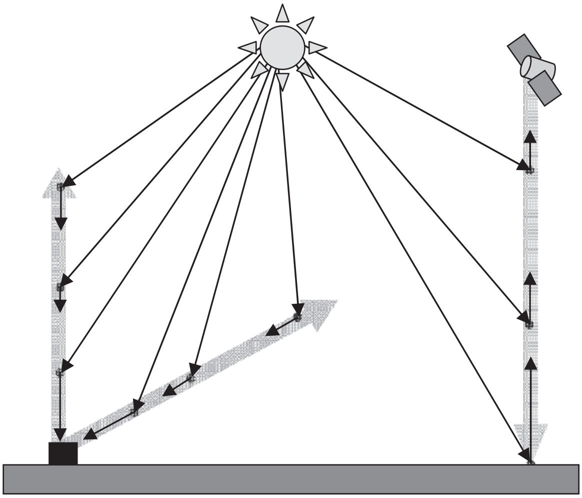

Fig. 9.3. Sketch of ground-based and satellite-borne passive DOAS observations

the nadir is at $\alpha = -90°$. The viewing direction can also be measured from the zenith, in which case viewing parallel to the ground is at a zenith angle of $\vartheta = 90°$ and the nadir is at $\vartheta = 180°$. The second angle that is important is the viewing azimuth angle, defined in the same way as for the solar position.

The zenith viewing geometry, i.e. $\alpha = 90°$ has historically been one of the most successful applications of passive DOAS. Many of the basic concepts of AMF calculations have been determined for this viewing geometry, mostly in the context of studying stratospheric trace gases and the chemistry leading to the Antarctic ozone hole.

As illustrated in Fig. 9.3, in zenith scattered light DOAS applications the irradiance received by the detector originates from light scattered by the air molecules and particles that are located along the viewing direction of the telescope. Assuming, for now, that only one scattering process occurs between the sun and the detector, one can gain a basic understanding of the zenith sky observations.

Figure 9.4 illustrates that two processes have to be taken into account to understand the measurement of radiances at the detector. First, one has to consider the efficiency by which solar light is scattered from its original direction towards the detector. Secondly, one needs to consider the extinction, either by trace gas absorption or by Rayleigh scattering, along the different light paths. The main process changing the direction of light under clear sky conditions is Rayleigh scattering in the zenith, which depends primarily on air density, i.e. the number of scattering air molecules. The scattering efficiency will thus be highest close to the ground and decrease exponentially

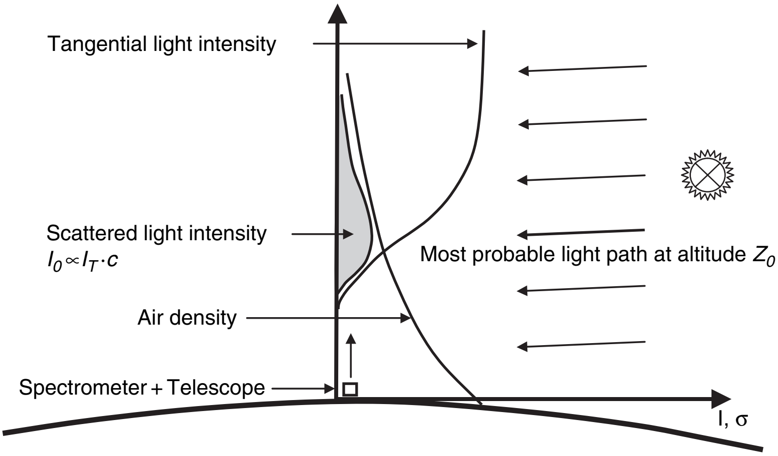

Fig. 9.4. Geometry of Zenith Scattered Light DOAS–radiation transport in the atmosphere. There is an infinite number of possible light paths. However, at solar zenith angles around 90° the light seen by the spectrometer most likely originates from a certain altitude range around z_i

with altitude. In a thin layer at height z', the intensity of light scattered towards the detector depends on the intensity reaching the scattering point, I_z, the Rayleigh scattering cross-section, σ_R, and the air density, $\rho(z)$ (Solomon et al., 1987):

$$I_S(\lambda, z') = I_0(\lambda, z') \cdot \sigma_R(\lambda) \cdot \rho(z')\, dz' \ . \tag{9.6}$$

The extinction along the light path will depend on the length of each light path in the atmosphere, the concentration of air molecules and, in the case of strong absorbers, the concentration of these gases.

$$I_S(\lambda, z) = I_0(\lambda, z) \times \exp\left(-\sigma_R(\lambda) \int_z^{\infty} \rho(z') \cdot A(z', \vartheta)\, dz' \right) \ , \tag{9.7}$$

where $A(z)$ is the direct sun AMF for the light before scattering at altitude z'. Because the AMF depends on the solar zenith angle, the length of each light path will also depend on the SZA, as can be seen in Fig. 9.1. This leads to a decrease in intensities I(z) with SZA. The dependence of Rayleigh scattering on air density indicates that the intensity reaching the zenith point at which it is scattered will be lowest close to the ground and increase with altitude.

Combining the two effects, which show opposite altitude dependences, gives rise to a distribution of scattered light intensity that is small at the ground, increases to a maximum, and then decreases again with altitude. The maximum of this scattered light distribution represents the most probable height that the observed light originates from. The contribution of scattering in a thin layer at altitude z to the intensity observed by the detector is then:

$$\begin{aligned} I_S(\lambda, z) = \sigma_R(\lambda) \cdot \rho(z) \cdot I_0(\lambda) \cdot \exp\left(-\sigma_R(\lambda) \int_z^{\infty} \rho(z') \cdot A(z', \vartheta)\, dz \right) \\ \times \exp\left(-\sigma_R(\lambda) \int_h^{z} \rho(z')\, dz' \right) \ . \end{aligned} \tag{9.8}$$

The last term in this equation is the Rayleigh extinction on the light path from the scattering height to the detector, which is assumed to be at an altitude h.

This equation allows the discussion of the dependence of scattering properties with the SZA. At large SZA, the light paths in the atmosphere become large, and at lower altitudes the intensity reaching the scattering height is reduced more than at higher altitudes (Fig. 9.5). The most probable scattering height, therefore, moves upwards as the SZA increases. The most probable scattering height also depends on the wavelength, due to the wavelength dependence of Rayleigh scattering. Z_o typically varies from about 26 km (327 nm) to 11 km (505 nm) at 90 deg SZA.

In the presence of an absorbing trace gas, (9.8) is expanded by including the absorption cross-section and the trace gas concentration at each height.

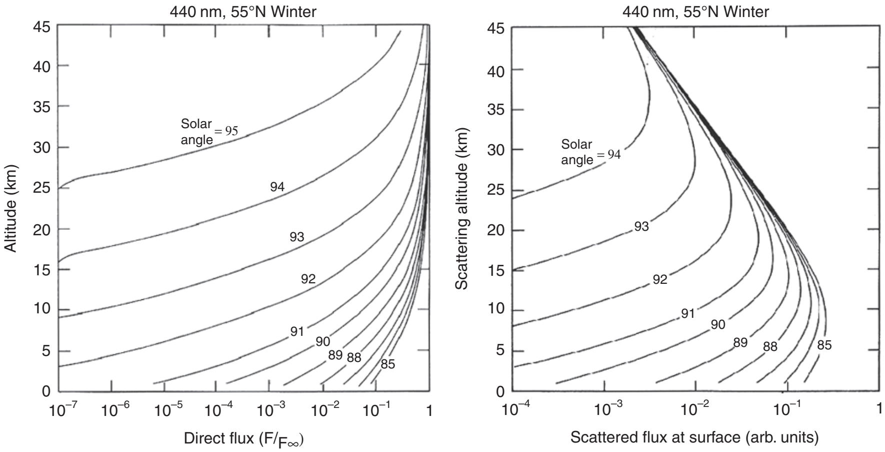

Fig. 9.5. Intensity of the direct (**left panel**) and scattered (**right panel**) radiative flux as a function of altitude for various SZA (from Solomon et al, 1987, Copyright by American Geophysical Union (AGU), reproduced by permission of AGU)

$$I_S^A(\lambda, z) = I_S(\lambda, z) \cdot \exp\left(-\sigma(\lambda) \int_z^\infty C(z') \cdot A(z', \vartheta)\, dz\right) \cdot \exp\left(-\sigma(\lambda) \int_h^z C(z')\, dz'\right) . \tag{9.9}$$

Because the large direct sunlight AMFs, $A(z', \vartheta)$, are approximately equal to $1/\cos\vartheta$, the absorption is largest at large SZAs. The slant light paths through the atmosphere are quite long under twilight conditions: at 90° zenith angle and 327 nm, the horizontal light path length through the stratosphere is 600 km. The AMFs for the path below the scattering height are, i.e. the second exponential term in (9.9), equal to unity.

Our discussion shows that the light reaching the detector is an average over a multitude of rays, each of which takes a somewhat different route through the atmosphere. The detector, therefore, measures the intensity-weighted average of the absorptions along the different light paths arriving at the telescope. This 'apparent' column density S is, for historic reasons, also called SCD, although it has no resemblance to the slanted column of direct solar measurements.

Based on our discussion above, we can now use the definition of SCD (9.3) to write down a simplified expression for SCD for scattered sunlight:

$$S(\vartheta) = \frac{1}{\sigma(\lambda)} \ln\left[\frac{\int_h^\infty I_S^A(\lambda, z) dz}{\int_h^\infty I_S(\lambda, z) dz}\right] . \tag{9.10}$$

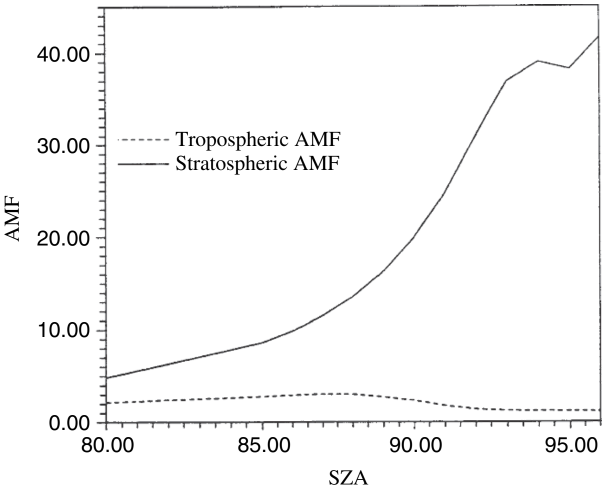

Fig. 9.6. Stratospheric and tropospheric AMF of NO_2 at 445 nm determined using a single scattering radiative transfer model (from Stutz, 1992)

This SCD can now be used in (9.4) to calculate the AMF for zenith scattered light. Figure 9.6 shows such an AMF for a stratospheric absorber at 450 nm. As expected, the AMF increases with SZA as the light path in the stratosphere becomes longer and the most probable scattering height moves upwards. The decrease at very large SZA occurs when Z_0 moves above the absorption height.

While our simplified description illustrates the principles of radiative transfer and AMF calculations, it is insufficient to make accurate AMF calculations. Other physical processes such as scattering by aerosol particles, refraction, and multiple scattering need to be considered in the AMF calculations. Interpretation of the SCD, therefore, requires radiation transport modelling. More details on atmospheric radiation transport are available in Chap. 4, and, for example, Solomon et al. (1987), Frank and Platt (1990), or Marquard et al. (2000). To put it simply, the detected light from the zenith can be represented by a most probable light path through the atmosphere defined by the most likely scattering height Z_o in the zenith.

9.1.3 Scattered Off-axis and Multi-axis AMF

Scattered-light DOAS viewing geometries other than the zenith have become increasingly popular in recent years. The motivation for using smaller elevation angles is twofold. With respect to stratospheric measurements, lower viewing angles can improve the detection limits by increasing the light intensity reaching the detector. The stronger motivation is the ability to achieve larger AMFs for tropospheric trace gases. To understand these motivations, the underlying radiative transfer principles are discussed here.

Our argument follows very closely the approach we have adopted for ZSL-DOAS in Sect. 9.1.2. The light of the detector originates from scattering processes within the line of view of the detector. Because the detector aims at lower elevations than in the ZSL case, i.e. the viewing path crosses through layers with a higher air density, scattering events closer to the ground will contribute more to the detected intensity. Consequently, the most probable scattering height will move downwards in the atmosphere as the viewing elevation angle decreases. It is typically somewhere in the troposphere for all wavelengths. We can now expand (9.8) and (9.9) by including an AMF, $A_T(z, \alpha)$, for the path between the scattering event and the detector. In an approximation based on purely geometrical arguments, $A_T(z, \alpha)$ is equal to $1/\cos\alpha$, i.e. it increases with decreasing viewing elevation angle. This will change the distribution of the scattering term in (9.9), as well as increase the Rayleigh extinction between the scattering event and the detector. It should be noted here that both the SZA and the elevation angle also influence σ_R (see Chap. 4).

$$\begin{aligned} I_S(\lambda, z, \alpha) = {} & \sigma_R(\lambda) \cdot \rho(z) \cdot A(z', \alpha) \cdot I_0(\lambda) \\ & \cdot \exp\left(-\sigma_R(\lambda) \int_z^{\infty} \rho(z') \cdot A_S(z', \vartheta)\, dz \right) \\ & \cdot \exp\left(-\sigma_R(\lambda) \int_h^{z} \rho(z') \cdot A_T(z', \alpha)\, dz' \right) . \end{aligned} \tag{9.11}$$

The smaller elevation angles also influence the absorption of trace gases. Equation (9.9) thus has to be expanded to include $A_T(z, \alpha)$ in the second integral:

$$\begin{aligned} I_S^A(\lambda, z, \alpha) = I_S(\lambda, z, \alpha) \cdot \exp & \left(-\sigma(\lambda) \cdot \int_z^{\infty} C(z') \times A_S(z', \vartheta)\, dz \right) \\ \cdot \exp & \left(-\sigma(\lambda) \cdot \int_h^{z} C(z') \cdot A_T(z', \alpha)\, dz' \right) . \end{aligned} \tag{9.12}$$

One can see that the lower elevation in our simplified model does not change the first integral that describes the light path before the scattering event. The behaviour of stratospheric trace gases, for example, does not depend on the elevation angle, while that of tropospheric trace gases will. The SCD for the off-axis case can now be calculated according to (9.10).

To address the separation of stratospheric and tropospheric absorbers in more detail, we will further simplify our discussion by concentrating on the most probable light path. This eliminates the integrations in (9.10) to calculate the SCD and the AMF. Figure 9.7 illustrates this simplified view of off-axis viewing geometries. In this simplified picture, the AMFs $A_S(z, \vartheta)$ and $A_T(z, \alpha)$ are independent of altitude z and can be approximated as $1/\cos\vartheta$

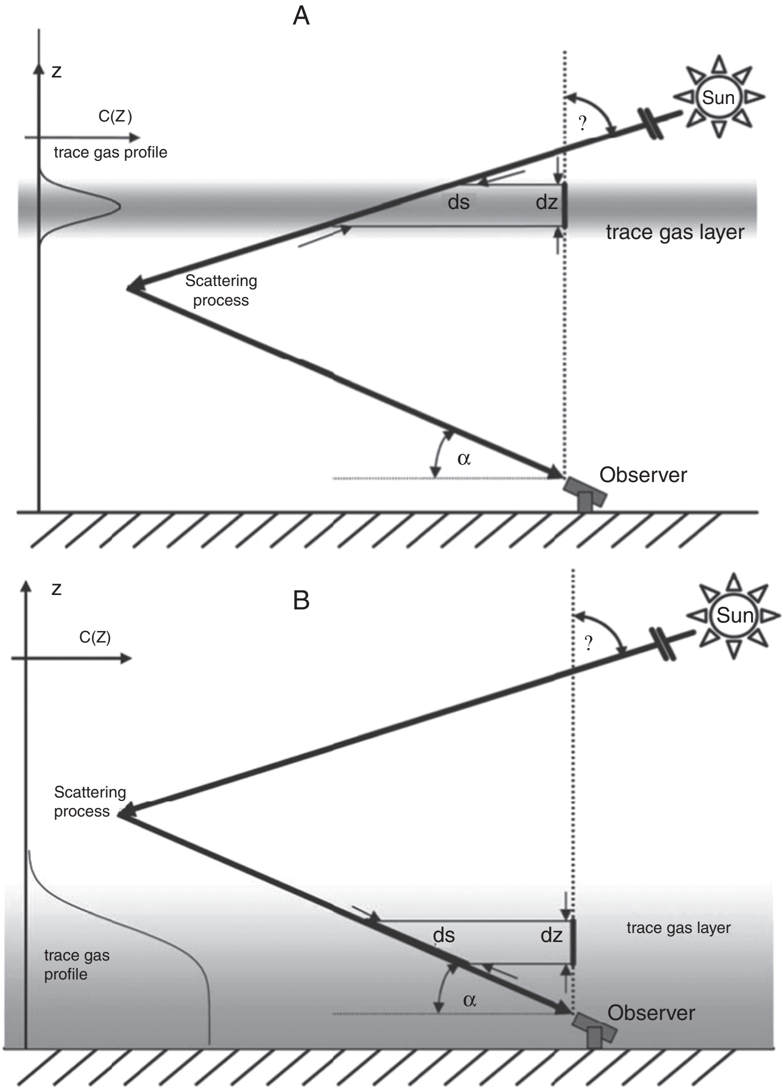

Fig. 9.7. Geometry of Off-axis DOAS and a sketch of the associated radiation transport in the atmosphere. Like in the case of ZSL-DOAS, there is an infinite number of possible light paths (from Hönninger, 1991)

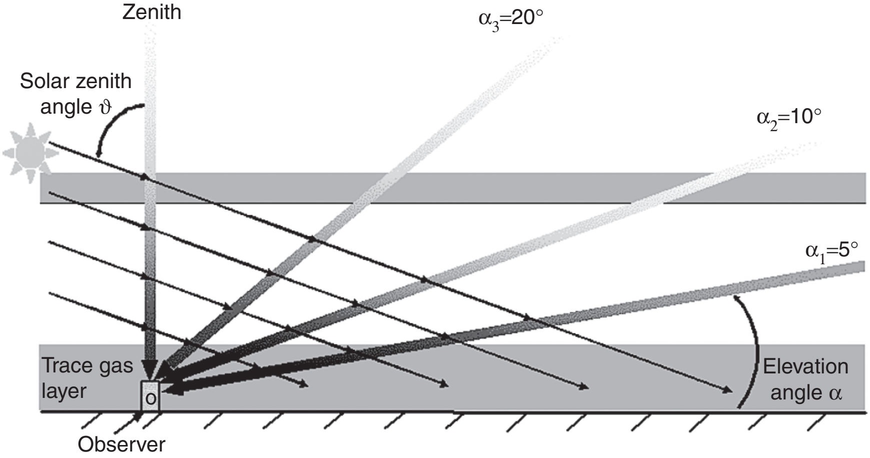

Fig. 9.8. Geometry of Multi-axis DOAS (MAX-DOAS) and a sketch of the associated radiation transport in the atmosphere. As in the case of ZSL-DOAS, there is an infinite number of possible light paths

and $1/\cos\alpha$, respectively. We further introduce the tropospheric and stratospheric vertical column densities, $\mathrm{VCD_T}$ and $\mathrm{VCD_S}$, which integrate the vertical trace gas concentration profile from the ground to the scattering altitude and from the scattering altitude to the edge of the atmosphere, respectively. After these simplifications, we find that the SCD can be described by:

$$S(\alpha,\vartheta) = V_T \cdot A_T(\alpha) + V_S \cdot A_S(\vartheta) = \frac{V_T}{\cos\alpha} + \frac{V_S}{\cos\vartheta}\,. \tag{9.13}$$

The SCD, therefore, depends both on the SZA, which controls the contribution of the stratospheric column, and the elevation angle, which controls the contribution of the tropospheric column.

While this equation illustrates the dependence of the SCD and the total AMF on the SZA, the elevation angle, and the vertical trace gas profile, it is highly simplified. In the case of low elevations, which are often used to increase the tropospheric path length, multiple scattering events, curvature of the earth, and refraction become significant (see Fig. 9.8). In addition, the higher levels of aerosols in the troposphere make Mie scattering an important process that must be included in the determination of AMF. To consider all these effects, a detailed radiative transfer model is required. A short description of such models will be given in Sect. 9.2.

9.1.4 AMFs for Airborne and Satellite Measurements

Airborne and satellite DOAS measurements have become an important tool to study atmospheric composition on larger scales. These measurements are based on scattered sunlight detection, and AMFs have to be calculated to interpret the observations. In principle, the approach is very similar to that shown for other scattered light applications.

As with the multi-axis approach, the SZA and the viewing angle have to be considered. In this case, however, the instruments look downwards and can, at least at higher wavelengths, see the ground. Besides the scattering on air molecules and aerosol particles, clouds and the albedo of the ground have to be considered. The ground is typically parameterised by a wavelength-dependent albedo and the assumption that the surface is a Lambertian reflector, or by a bi-directional reflectivity function (BDRF), which parameterises the reflection based on incoming and outgoing reflection angles. Clouds seen from an airplane or a satellite can be parameterised by introducing parallel layers of optically thick scatterers in a multiple scattering model or, in the case of thick clouds, by parameterising them as non-Lambertian reflectors in the model at a certain altitude (Kurosu et al., 1997).

An additional problem, which we will not discuss here in detail, is the fact that downward-looking airborne or satellite instruments often observe areas of the earth's ground that may also be partially covered by clouds. The spatial averaging over the earth surface together with clouds is a challenge for any radiative transfer model.

9.1.5 Correction of Fraunhofer Structures Based on AMFs

A challenge in applying DOAS to the measurement of atmospheric trace gases is the solar Fraunhofer structure, which manifests itself as a strong modulation of $I_0(\lambda)$ due to absorption in the solar atmosphere (see Chap. 6). We will discuss two approaches to overcome this problem, one for the measurement of stratospheric trace gases and one for the measurement of tropospheric gases. Both techniques are based on the choice of suitable Fraunhofer reference spectra that can be used in the analysis procedures described in Chap. 8, or in simple terms by which the observed spectrum is divided. Ideally, one would like to choose a spectrum without any absorption of the respective atmospheric trace gas. Since this is not possible, both techniques rely on the choice of a Fraunhofer reference spectrum where the trace gas absorptions are small. Based on our discussion in Sect. 9.1.5, this is equivalent to a small AMF in the reference spectrum as compared to the actual observation.

In the case of ZSL measurements of stratospheric trace gases, our earlier discussions revealed that the AMF increases with the solar zenith angle. The obvious choice for a Fraunhofer reference spectrum is a spectrum measured at small SZA. Ideally, the ratio of a spectrum taken at a higher SZA, for example at sunset, and the Fraunhofer spectrum will consist of pure trace gas absorptions. The ratio of (9.9) for two different SZAs would eliminate the solar intensity, i.e. $I_S(\lambda, z)$. However, this approach poses another challenge since the division also eliminates the absorptions that are originally in the Fraunhofer reference spectrum, which are not known. The analysis of the ratio between the two spectra results in the so-called differential slant column density (DSCD), S', which is the difference between the SCDs of high SZA, ϑ_2, and the reference spectrum measured at low SZA ϑ_1:

$$S' = S(\vartheta_2) - S(\vartheta_1)\ . \tag{9.14}$$

A determination of the VCD is not directly possible from S'. A solution to this problem presents itself if the vertical column density of the absorbing trace gas remains constant with time, i.e. same at ϑ_2 and ϑ_1. Equation (9.14) can then be written as:

$$S' = S'(\mathrm{AMF}) = \mathrm{V} \times \mathrm{A}(\vartheta_2) - \mathrm{S}(\vartheta_1) \tag{9.15}$$

This linear equation can then be used to determine the VCD and $\mathrm{S}(\vartheta_1)$ by plotting the DSCD against the AMF and applying a linear fit to the resulting curve. An example of this so-called **Langley Plot** is shown in Fig. 9.9. The slope of the curve gives the VCD, while the extrapolation to $A = 0$ results in an ordinate intersection at $-S_0$.

In the case where the interest is more in tropospheric trace gases, the above method will not lead to the desired result since the tropospheric AMF is only weakly dependent on the SZA. However, as shown in Sect. 9.1.3, changing the

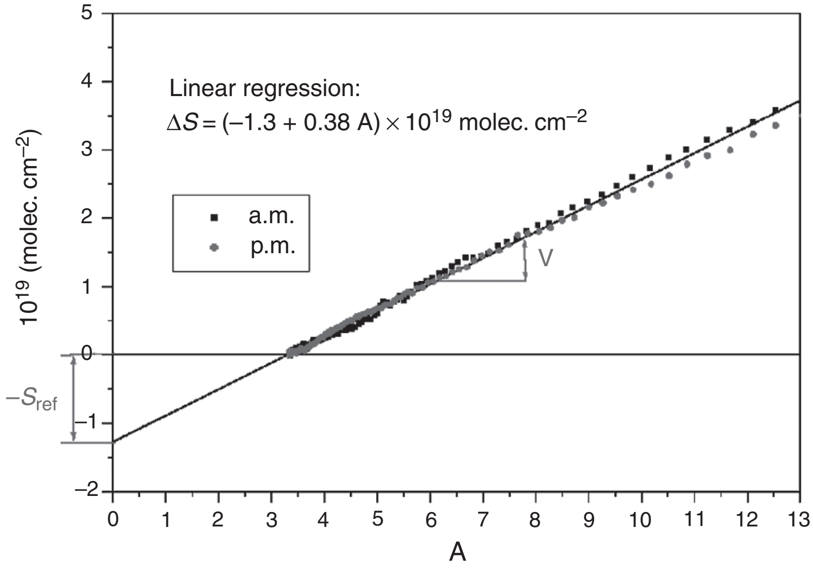

Fig. 9.9. Sample Langley plot: Measured ozone differential slant columns (DSCDs) are plotted as a function of the airmass factor A calculated for the solar zenith angle of the measurement. The slope of the plot indicates the vertical column density V. The ordinate section indicates the slant column density in the solar reference spectrum, S_{ref}

viewing elevation will considerably influence the tropospheric AMF (9.13). The approach to measure tropospheric gases is thus to use a zenith spectrum ($\alpha = 90°$) as the Fraunhofer reference to analyse spectra measured at lower elevations. To guarantee that the stratospheric AMF is the same for these two spectra, one has to measure the zenith and the low elevation spectrum simultaneously, or at least temporally close together. Using (9.13), this approach describes:

$$S' = S(\alpha, \vartheta) - S(90, \vartheta) = V_T \times A_T(\alpha) \, . \tag{9.16}$$

It should be noted that, despite the fact that we have called V_T the tropospheric vertical column density, the height interval over which the vertical concentration profile is integrated in V_T depends on the radiative transfer. Typically V_T does not cover the entire troposphere, but rather the boundary layer and the free troposphere. A more detailed discussion of this will be given in Sect. 9.3.

The dependencies described in (9.13) gave rise to a new method that uses simultaneous measurements of one or more low-viewing elevations, together with a zenith viewing channel to measure tropospheric trace gases. This multi-axis DOAS method is described in detail in Sect. 9.3.3.

9.1.6 The Influence of Rotational Raman scattering, the 'Ring Effect'

Named after Grainger and Ring [1962], the Ring effect, it manifests itself by reducing the optical density of Fraunhofer lines observed at large solar zenith angles (SZA), compared to those at small SZAs. This reduction is on the order of a few percent. However, because atmospheric trace gas absorptions can be more than an order of magnitude smaller than the Ring effect, an accurate correction is required.

Several processes, such as rotational and vibrational Raman scattering, aerosol fluorescence, etc. have been suggested as explanations of the Ring effect. Recent investigations [Bussemer 1993, Fish and Jones 1995, Burrows et al. 1995, Joiner et al. 1995, Aben et al. 2001] show convincingly that rotational Raman scattering is the primary cause of the Ring effect.

In short, light intensity scattered into a passive DOAS instrument can be expressed as:

$$I_{meas} = I_{Rayleigh} + I_{Mie} + I_{Raman} = I_{elastic} + I_{Raman}$$

The accurate determination of $\mathrm{I}_{\mathrm{elastic}}$ and $\mathrm{I}_{\mathrm{Raman}}$ requires detailed radiative transfer calculations for each observation. However, Schmeltekopf et al. [1987] proposed an approximation which is based on the inclusion of a "Ring Spectrum" in the spectral analysis of the observations (see Chap. 8).

Based on the logarithm of the measured spectrum, $\ln(\mathrm{I}_{\mathrm{meas}})$, and the equation above the following approximation can be made.

$$\begin{aligned}\ln(I_{meas}) &= \ln\left(I_{elastic}\cdot\frac{I_{elastic}+I_{Raman}}{I_{elastic}}\right)\\ &= \ln(I_{elastic}) + \ln\left(1+\frac{I_{Raman}}{I_{elastic}}\right) \approx \ln(I_{elastic}) + \frac{I_{Raman}}{I_{elastic}},\end{aligned}$$

where the ratio of the Raman and the elastic part of the intensity is considered the Ring spectrum:

$$I_{Ring} = \frac{I_{Raman}}{I_{elastic}}$$

This approximation has been proven to be simple and effective. An experimental and a numerical approach exist to determine a Ring spectrum.

1) The first approach is based on the different polarization properties of atmospheric scattering processes. Rayleigh scattering by air molecules is highly polarized for a scattering angles near 90° (see Chap. 4, Sect. 4.2.2). Light scattered by rotational Raman scattering, on the other hand, is only weakly polarized (see Sect. 4.2.3). By measuring the intensity of light polarized perpendicular and parallel to the scattering plane, the rotational

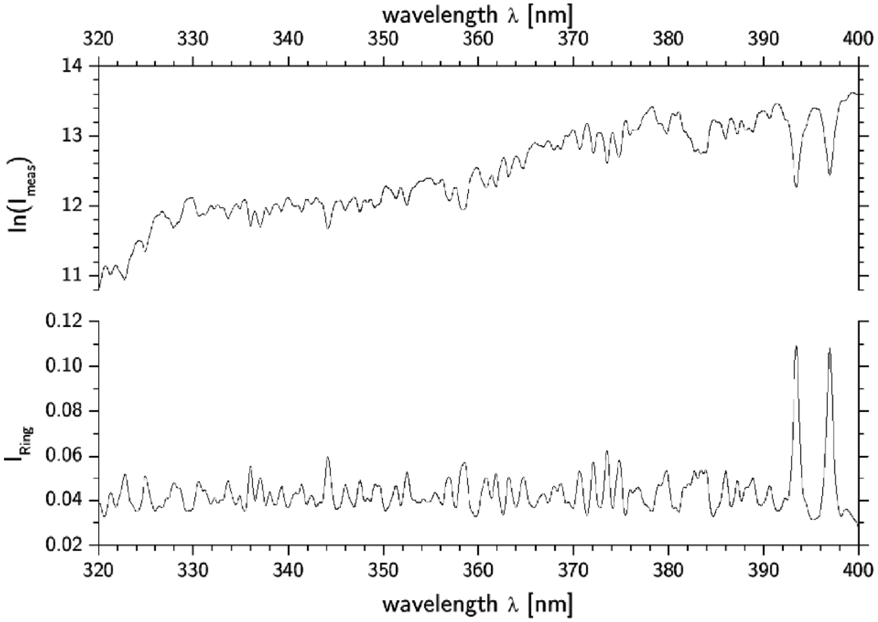

Fig. 9.10. Sample Ring spectrum (I($_{Ring}$)) calculated for the evaluation of UV spectra taken during ALERT2000. Shown is also the logarithm of the Fraunhofer reference spectrum(I$_{meas}$) used for the calculation. The spectrum was taken on April 22, 2000 at 15:41 UT at a local solar zenith angle of 70° and zenith observation direction (from Hönninger, 2001)

Raman component, and therefore a "Ring spectrum", can be determined [Schmeltekopf et al. 1987, Solomon et al. 1987].

This approach faces a number of challenges. Mie scattering also contributes to the fraction of non-polarized light in the scattered solar radiation. The presence of aerosol or clouds therefore makes the determination of the Ring spectrum difficult. Also, the atmospheric light paths for different polarizations may be different, and can thus contain different trace gas absorptions, which can affect the DOAS fit of these gases.

2) The second approach uses the known energies of the rotational states of the two main constituents of the atmosphere, O_2 and N_2, to calculate the cross section for rotational Raman scattering. This can be realized, either by including Raman scattering into radiative transfer models [e.g. Bussemer 1993; Fish and Jones 1995; Funk 2000], or by calculating the pure ratio of the cross sections for Raman and Rayleigh scattering. In many realizations this calculation is based on measured Fraunhofer spectra (e.g. MFC [Gomer et al. 1993]) leading to a Raman cross section which has all the spectral characteristics of the respective instrument. The rotational Raman spectrum is then divided by the measured Fraunhofer spectrum to determine the Ring spectrum (Fig. 9.10). Note, the Fraunhofer spectrum must be corrected for rotational Raman scattering to represent pure elastic scattering. In most cases, this approach leads to an excellent correction of the Ring effect.

9.2 AMF Calculations

The detailed calculation of AMFs requires the consideration of different physical processes influencing the radiative transfer (RT) in the atmosphere. Scattering processes, either Rayleigh or Mie scattering, reflection on the earth's surface, refraction, the curvature of the earth, and the vertical distribution of trace gases play a role in the transfer of solar radiation. Consequently, sophisticated computer models are employed to calculate the RT in the atmosphere and the AMFs needed to retrieve vertical column densities from DOAS observations of scattered sun-light.

It is beyond the scope of this book to describe the details of RT models that are currently in use for AMF calculations. The interested readers can find details of RT modelling in Solomon et al. (1987), Perliski and Solomon (1992), Perliski and Solomon (1993), Stamnes et al. (1988), Dahlback and Stamnes (1991), Rozanov et al. (1997), Marquard (1998), Marquard et al. (2000), Rozanov et al. (2000), Rozanov (2001), Spurr (2001), and v. Friedeburg (2003).

However, we give a short overview of the most commonly used RT methods and the input data required to run these models.

The traditional computation procedure for the calculation of AMFs for a certain absorber is straightforward (e.g. Frank, 1991; Perliski and Solomon, 1993). For this purpose, the following computation steps are performed:

1. The radiances $I_{\mathrm{S}}(\lambda, 0)$ and $I_{\mathrm{S}}{}^{\mathrm{A}}(\lambda, \sigma)$ are calculated by an appropriate RT model. This means that two model simulations must be performed: one simulation where the absorber is included and one simulation where the absorber is omitted from the model atmosphere.
2. The slant (or apparent) column density S is calculated according to the DOAS method, i.e. (9.1).
3. The vertical column density is calculated by integrating the number density of the considered absorber, which has been used as an input parameter for the modelling of $I_{\mathrm{S}}{}^{A}(\lambda, \sigma)$ in step 1, in the vertical direction over the spatial extension of the model atmosphere.
4. The AMF is then derived according to (9.4).

This computational procedure is used to calculate AMFs when multiple scattering is taken into consideration and was also used in some single-scattering RT models. It was first described and applied by Perliski and Solomon (1993). At present, it appears to be implemented in all existing RT models that consider multiple scattering, such as discrete ordinates radiative transfer (DISORT) models (Stamnes et al., 1988; Dahlback and Stamnes, 1991), GOMETRAN/SCIATRAN (Rozanov et al., 1997), AMFTRAN (Marquard, 1998; Marquard et al., 2000), the integral equation method RT models (Anderson and Lloyd, 1990), and the backward Monte Carlo RT models (e.g. Perliski and Solomon, 1992; Marquard et al., 2000). We refer to this method as the 'traditional' (linear) AMF computation method.

There is a second method to calculate AMFs, which was often used for single-scattering radiative transport models. In this approximation, it is assumed that the radiation propagating through the atmosphere is scattered once before it is detected. It is evident that this scattering process must occur along the detector's viewing direction. Mainly, some of the earlier single-scattering RT models apply this method (see Sarkissian et al., 1995; and references therein). The method is based on a linear weighting scheme (see e.g. Solomon et al., 1987), and thus there is a second assumption entering into this method, namely, that the total optical density at the detector position is equivalent to the sum of the optical densities along the single paths weighted by their probabilities. However, this is, in general, not valid if there are several paths through the atmosphere, which is the case for measurements of scattered radiation.

9.2.1 Single-scattering RT Models

Earlier RT models considered only one scattering event in the atmosphere, and were thus termed 'single-scattering models'. Figure 9.11 illustrates the approach most often taken in these simple RT models. The curved atmosphere

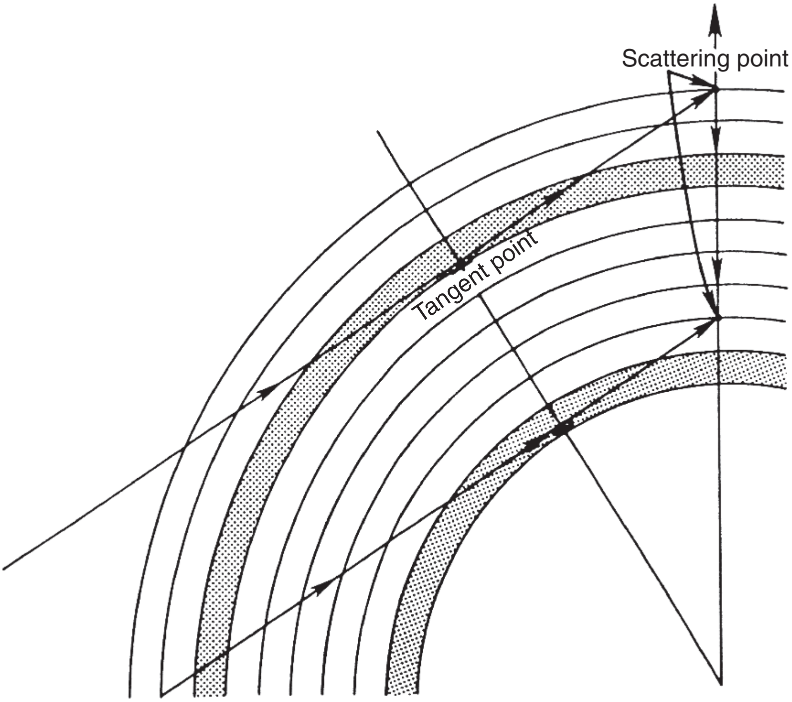

Fig. 9.11. Definition of the tangent point in spherical geometry (from Perliski and Solomon, 1993, Copyright by American Geophysical Union (AGU), reproduced by permission of AGU)

is subdivided in distinct layers. Light travels from the direction of the sun, defined by the SZA, through the atmosphere until it reaches the zenith over the DOAS instrument. At the zenith, a parameterisation of Rayleigh scattering and Mie scattering is used to calculate the fraction of light scattered towards the earth surface from this scattering point (Fig. 9.12). The vertical profiles of air density and aerosol concentration which are needed both for the calculation of extinction along the light path and the scattering efficiency at the scattering point, are input parameters of the model. Refraction is considered whenever a ray enters a new layer following Snell's law. Absorption is calculated from the path length in each layer, vertical concentration profile, and absorption cross-section supplied to the model. The model then performs a numeric integration of (9.10) to derive the SCD for each SZA and wavelength. The ratio of this SCD with the VCD calculated from the vertical trace profile is then the desired AMF.

A number of single-scattering models have been developed over the years (Frank, 1991; Perliski and Solomon, 1993; Schofield et al., 2004). The advantage of these models is their simplicity and the lesser use of computer resources. Perliski and Solomon (1993) discuss the disadvantages of these models. In particular, the omission of multiple scattering events poses a

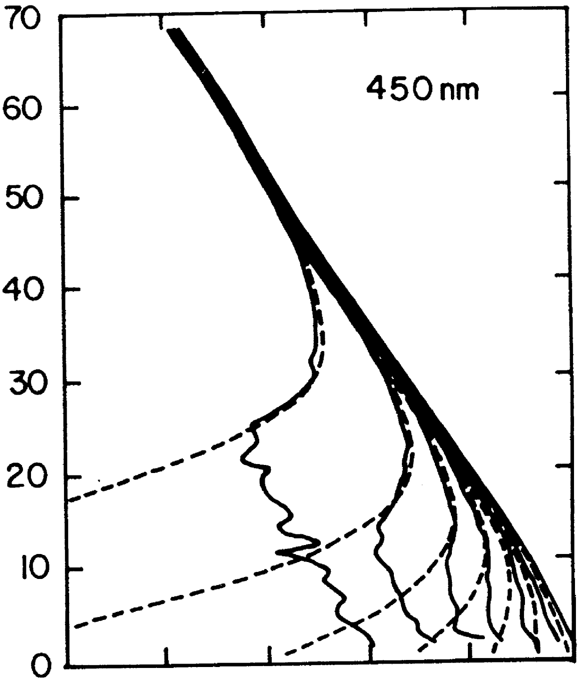

Fig. 9.12. Contribution of different altitudes to the intensity detected by a ground-based ZSL-DOAS instrument for different SZA. The dashed and solid lines show results from a single and a multiple scattering model, respectively. (from Perliski and Solomon, 1993, Copyright by American Geophysical Union (AGU), reproduced by permission of AGU)

serious challenge. Figure 9.12 illustrates the change in the contribution of each altitude to the detected intensity for different SZA. In particular in the lower atmosphere, the contribution of multiple scattering cannot be ignored. This effect is even more severe if off-axis geometries are used, where the most probable scattering height is in the troposphere. Multiple scattering also has to be considered when high aerosol levels are encountered. For these reasons, single-scattering models are rarely used.

9.2.2 Multiple-scattering RT Models

Radiative transfer models that consider multiple scattering events are the standard in current AMF calculations. A common approach to these calculations is to solve the RT equations described in Chap. 3 for direct and diffuse radiation. Several implementations for the numerical solution have been brought forward over the past years. Rozanov et al. (2000, 2001) describe a combined differential-integral (CDI) approach that solves the RT equation in its integral form in a pseudo-spherical atmosphere using the characteristics method. The model considers single scattering, which is calculated truly spherical and multiple scattering, which is initialised by the output of the pseudo-spherical model. This model is known as SCIATRAN (http://www.iup.uni-bremen.de/sciatran/).

Other models are based on the discrete ordinate method to solve the RT equation. In this approach, the radiation field is expressed as a Fourier cosine series in azimuth. A numerical quadrature scheme is then used to replace the integrals in the RT equation by sums. The RTE equation is, therefore, reduced to a set of coupled linear first-order differential equations, which are consequently solved (Lenoble, 1985; Stamnes et al., 1988; Spurr, 2001). This model also employs a pseudo-spherical geometry for multiple scattering in the atmosphere.

A number of RT models rely on the Monte Carlo method, which is based on statistical sampling experiments on a computer. In short, RT is quantified by following a large number of photons as they travel through the atmosphere. While in the atmosphere, the photons can undergo random processes such as absorption, Rayleigh scattering, Mie scattering, reflection on the ground, etc. For each of these processes, a probability is determined, which is then used to randomly determine if, at any point in the atmosphere, the photon undergoes a certain process. A statistical analysis of the fate of the photon ensemble provides the desired RT results. More information on Monte Carlo methods can be found in Lenoble (1985). While the most logical approach to implement Monte Carlo methods for AMF calculations is to follow photons entering the atmosphere and counting them as they arrive at the detector, this ‘forward Monte Carlo’ method is slow and numerically inefficient. Consequently, it is not used for this specific application. However, the ‘backward Monte Carlo method’, in which photons leave the detector and are then traced through the atmosphere, has proven to be a reliable approach to calculate AMFs (Perliski and Solomon, 1993; Marquard et al., 2000; von Friedeburg et al., 2003). The advantage of Monte Carlo methods is their precise modelling of RT without the need for complex numerical solutions or the simplifications of the underlying RT equation (Chap. 4). The disadvantage, however, is that Monte Carlo models are inherently slow due to the large number of single-photon simulations that are needed to determine a statistically significant result.

9.2.3 Applications and Limitations of the ‘Traditional’ DOAS Method for Scattered Light Applications

The classical DOAS approach has been widely and successfully applied to measurements of scattered sun-light. It uses the same tools as described in Chaps. 6 and 8. In short, based on Lambert–Beer’s law:

$$I(\lambda) = I_0(\lambda) \cdot \exp\left(-\sigma(\lambda) \cdot c \cdot L\right) \ , \tag{9.17}$$

one can calculate the product of path length and concentration of a trace gas, i.e. the column density, by measuring $I(\lambda)$ and $I_0(\lambda)$ and using the known absorption cross-section of the gas $\sigma(\lambda)$.

$$c \cdot L = -\frac{1}{\sigma(\lambda)} \ln \left(\frac{I(\lambda)}{I_0(\lambda)} \right) . \tag{9.18}$$

Most applications of scattered light DOAS follow this approach by using the measurement in the zenith or at a low elevation angle as $I(\lambda)$ and, as described above, a spectrum with small SZA or different elevation angle for $I_0(\lambda)$. In this case, the fitting of one or more absorption cross-sections modified to the instrument resolution will yield the SCD, or more precisely the DSCD. It is also clear that the SCD is independent of the wavelength. This appears to be trivial here. However, we will see below that this may not be the case for certain scattered light measurements.

In this section we argue that this classical DOAS approach can lead to problems in the analysis of scattered light applications. To simplify the discussion, we assume that $I_0(\lambda)$ is the solar scattered light without the presence of an absorber as already assumed in Sect. 9.1. The discussion can easily be expanded to the case where a different solar reference spectrum is used (see Sect. 9.1.5).

We will use a simplified version of (9.10), where we replace the integrals over height with integrals over all possible light paths that reach the detector. In addition, we simplify this equation further by replacing the integrals with a SCD for each path, S'. As assumed in the classical approach, the left side of the equation is the desired VCD times the AMF, the SCD determined by DOAS measurements.

$$V \cdot A = \frac{1}{\sigma(\lambda)} \ln \left[\frac{\int\limits_{all\,paths} I_S(\lambda, z) \cdot \exp\left(-\sigma(\lambda) \cdot S'\right) dz}{\int\limits_{all\,paths} I_S(\lambda, z) dz} \right] . \tag{9.19}$$

The comparison with (9.10) reveals that the application of the logarithm is not as straightforward as in the case of Lambert–Beer's law. The logarithm has to be applied on the integrals over the intensities of the light passing the atmosphere on different light paths. We can now distinguish three cases to further interpret this equation:

1. In the case that SCD S' is the same for all paths, i.e. in case of direct solar measurements, the exponential function in the numerator can be moved in front of the integral and we have the classical Lambert–Beer's law. In this case, the methods described in Chap. 8, i.e. fitting of absorption cross-section, can be applied.
2. If we assume that the exponential function in the numerator of (9.19) can be approximated using $\exp(x) \approx 1 + x$, for $-\varepsilon < x < \varepsilon$, which is the case for a weak absorber, we can perform the following approximation:

$$\begin{aligned}
&\int\limits_{all\,paths} I_S(\lambda)\cdot\exp\left(-\sigma(\lambda)\cdot S'\right) \approx \int\limits_{all\,paths} I_S(\lambda)\cdot\left(1-\sigma(\lambda)\cdot S'\right) = \\
&= \int\limits_{all\,paths} I_S(\lambda) - \sigma(\lambda)\cdot \int\limits_{all\,paths} I_S(\lambda)\cdot S' \\
&= \left[\int\limits_{all\,paths} I_S(\lambda)\right]\cdot\left(1-\sigma(\lambda)\cdot\bar{S}\right) \quad with \quad \bar{S} = \frac{\int\limits_{all\,paths} I_S(\lambda)\cdot S'}{\int\limits_{all\,paths} I_S(\lambda)}. \\
&\approx \left[\int\limits_{all\,paths} I_S(\lambda)\right]\cdot\exp\left(-\sigma(\lambda)\cdot\bar{S}\right)
\end{aligned}$$

In the case of a weak absorber, i.e. typically with an optical density below 0.1, the classical approach can still be employed since the absorption cross-section $\sigma(\lambda)$ is now outside of the integral. The SCD $\bar{S}$ is the intensity-weighted average of all slant columns on different paths. One can, therefore, use the fitting of an absorption cross-section and a classical AMF for the analysis of the data.

3. In the case of a strong absorber (OD > 0.1), such as ozone in the ultraviolet wavelength region, the approximation used above cannot be employed. The RT in the atmosphere cannot be separated from the trace gas absorption. The integral in the numerator of (9.19) now becomes dependent on $\sigma(\lambda)$ through absorptions along each path, as well as the weighing of each path during the integration, i.e. paths with stronger absorptions have a smaller intensity and thus contribute less to the integral than paths that have weaker absorptions.

Richter (1997) investigated this effect and found that the classical approach introduces small VCD errors of ~2% for ozone absorptions in the ultraviolet for SZAs below 90° in ZSL applications. However, the VCD error can reach 15% if the classical DOAS approach is used for SZAs above 90° in this wavelength region. For ozone in the visible and NO_2, the error generally remains below 2% for all SZA. Richter (1997) also showed that in the UV above 90° SZA, the residual of the fit increases due to this effect. He proposes an extended DOAS approach, which instead of using absorption cross-sections in the fitting procedure uses wavelength-dependent slant column optical densities extracted from a RT model.

An additional problem in the use of the DOAS approach for solar measurements is the temperature dependence of absorption sections. Because the light reaching the detector crosses the entire atmosphere, absorption occurs at different temperatures found at different altitudes. Equation (9.19), therefore, needs to be expanded by introducing a temperature dependent $\sigma(\lambda, T)$. The light path through the atmosphere, i.e. the RT, now plays an important role since regions with different temperatures are weighted differently. Again, the solution of this problem lies in the combination of RT and absorption spectroscopy (Marquard et al., 2000).

9.3 AMFs for Scattered Light Ground-Based DOAS Measurements

The analysis of scattered light DOAS observations relies on the principles outlined earlier. However, the different observational setups require analysis strategies adapted to the particular geometry of each application. Central problems include the dependence of the radiation transport, and thus the AMFs, on the – a-priori unknown – amount of Mie scattering and the location of trace gases in the atmosphere. Here we discuss how AMFs depend on various atmospheric parameters, such as the solar position, the trace gas profile, etc., and how this impacts the analysis of DOAS observations.

9.3.1 ZSL-DOAS Measurements

Zenith scattered light applications have been and still are widely used to study stratospheric chemistry. The AMF can vary widely as a function of wavelength, trace gas absorption, vertical trace gas profile, and stratospheric aerosol loading (e.g. Solomon et al., 1987; Perliski and Solomon, 1993; Fiedler et al., 1994). On the other hand, tropospheric clouds are of comparatively little influence, thus making ground-based measurements by this technique possible when the SZA is smaller than 95°.

Dependence on SZA

For SZAs smaller than 75°, the AMF can be approximated by $1/\cos\vartheta$. At larger SZA, a RT model yields results as shown in Fig. 9.13 for ozone. The AMF increases continuously, reaching a value of 6–20 at 90° SZA, depending on the wavelength.

A small dip around 93° is caused by the most likely scattering height passing above the altitude of the stratospheric absorption layer, leading to a reduction of the effective path length. Wavelengths above 550 nm do not show this effect since the influence of scattering and absorption processes in the atmosphere, which also contribute, decrease as the wavelength increases.

Dependence on Solar Azimuth

The dependence of the AMF on the solar azimuth is generally small for ZSL appications. The only exception is when the stratospheric trace gas or aerosol is not homogeneously distributed, and the changing effective viewing direction causes a change in the parameters influencing the RT.

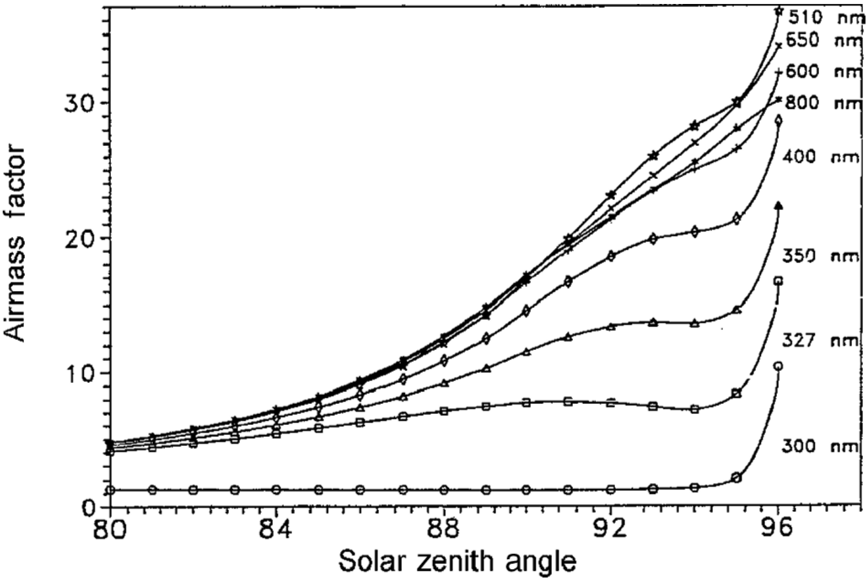

Fig. 9.13. Examples of Zenith Scattered Light (ZSL) airmass factors (AMFs) for stratospheric ozone and different wavelength as a function of solar zenith angles (in degrees) (from Frank, 1991)

Dependence on Wavelength

The ZSL-AMF depends on wavelength in the same way as Rayleigh and Mie scattering, as well as certain trace gas absorptions, are wavelength dependent. Figure 9.14 shows the dependence of the ozone AMF on the wavelength. The most notable feature is a steep increase of the AMF at lower wavelength. This is predominantely caused by the wavelength dependence of Raleigh scattering, which influences the weighing of the absorption layer.

A minimum around 570 nm is caused by the Chappuis ozone absorption band, which increases in strength at increasing SZA.

Dependence on Trace Gas Profile

The AMF also depends on the vertical profile of the respective trace gas. As illustrated in Fig. 9.4, the light collected at the ground is weighted towards a distribution around the most probable scattering angle. A trace gas profile with a maximum at this altitude will lead to a larger AMF than a profile with a maximum above or below the most probable scattering altitude, because the maximum of the profile is more heavily weighted. An extreme example for the dependence of the vertical profile is a comparison of the ZSL AMF of a trace gas located in the troposphere and the stratosphere. Figure 9.6 shows that the stratospheric AMF, for example for NO_2 around 445 nm, increases

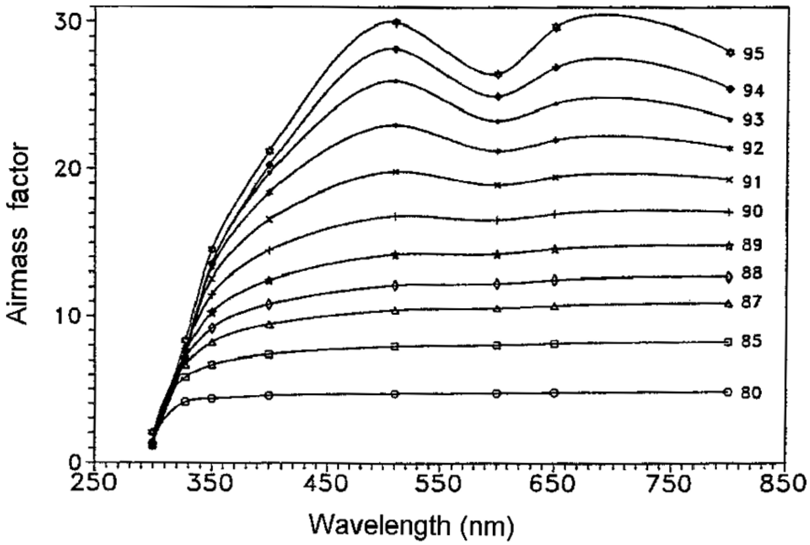

Fig. 9.14. Examples of Zenith Scattered Light (ZSL) airmass factors (AMFs) for stratospheric ozone and different solar zenith angles (in degrees) as a function of wavelength (from Frank 1991)

from 6 at 80° SZA to 20 at 90° SZA. In contrast, the tropospheric AMF is much smaller with a value of 2 at 80° SZA and ∼1 at 90° SZA. The much smaller values of the tropospheric AMF are due to the relatively small amount of light being scattered in the troposphere and the short path on which light scattered in the stratosphere passes through the troposphere. Above 90° SZA, less and less light is scattered in the troposphere, and the tropospheric AMF approaches 1 as stratospheric light passes the troposphere vertically.

Dependence on the Aerosol Profile

Aerosol particles have an influence on the RT since they efficiently scatter solar light into the receiving instrument. The impact on the AMF depends on the vertical distribution of aerosol and its scattering coefficient. For example, a stratospheric aerosol layer located below the maximum concentration of a stratospheric trace gas will lead to a reduction of the AMF since the most probable scattering altitude is shifted downwards. On the other hand, the AMF can, theoretically, be increased if an aerosol layer and a trace gas layer are collocated. The most prominent example of the impact of aerosol on AMF occured during the 1992 volcanic eruption of Mount Pinatubo. Since the volcanic aerosol was located below the ozone layer, the AMF were changed up to 40% relative to the pre-eruption case (e.g. Dahlback et al., 1994).

Tropospheric aerosol has little influence on the ZSL-AMF of a stratospheric trace gas, in particular at high SZA, since most of the scattering events occur in the stratosphere. Similarly, tropospheric clouds have little influence.

Chemical Enhancement

An additional problem in the AMF determination is found when measuring photoreactive species that change their concentration according to solar radiation (e.g. Roscoe and Pyle, 1987). Examples of such species are NO_2 and BrO. Because their concentration and vertical profile change during sunrise and sunset, the temporal change in these parameters have to be considered when calculating the AMF dependence on the SZA. This is typically achieved by using correction parameters derived from a photchemical model of stratospheric chemistry.

Accuracy of AMF Determinations

The accuracy of the AMF calculations directly affects the accuracy of the VCDs derived by ZSL–DOAS instruments. Much effort thus has gone into comparing RT models (Sarkissian et al., 1995; Hendrick et al., 2004, 2006).

Hendrick et al. (2006), for example, compared six RT models to determine the systematic difference between different solutions to the ZSL-DOAS retrieval. The models included single-scattering models, multiple-scattering models based on DISORT, CDIPI, or similar analytical approaches, and one Monte Carlo model. All models were constrained with the same boundary conditions, which included time-dependent profiles of the photoreactive trace gases BrO, NO_2, and OClO to describe chemical enhancement. Figure 9.15 shows a comparison of the models run in single scattering (SS) and multiple scattering (MS) mode. Note that the figure shows the SCD calculated by the models rather than the AMF. For BrO and OClO, the different models agreed better than ±5%. The agreement for NO_2 is ±2% for all, except one model. There is a systematic difference between SS and MS models, in particular for OClO, for which the altitude of the aerosol is similar to that of the OClO layer. These results show the typical systematic uncertainty of current RT models for ZSL-DOAS interpretation. It should be noted that this intercomparison does not take into account uncertainties introduced by the errors in the aerosol profile, trace gas profile, and chemical enhancement used for the retrieval of real ZSL-DOAS observations.

9.3.2 Off-axis-DOAS Measurements

As discussed in Sect. 9.1.3, a change of viewing direction can be beneficial for scattered light DOAS measurements in various respects. For example, Sanders et al. (1993) observed stratospheric OClO over Antarctica during twilight using an 'off-axis' geometry. Because the sky is substantially brighter towards the horizon in the direction of the sun at large SZAs, the signal-to-noise ratio of the measurements can be considerably improved as compared to zenith geometry. Sanders et al. (1993) also pointed out that the off-axis geometry increases the sensitivity for lower absorption layers. They found

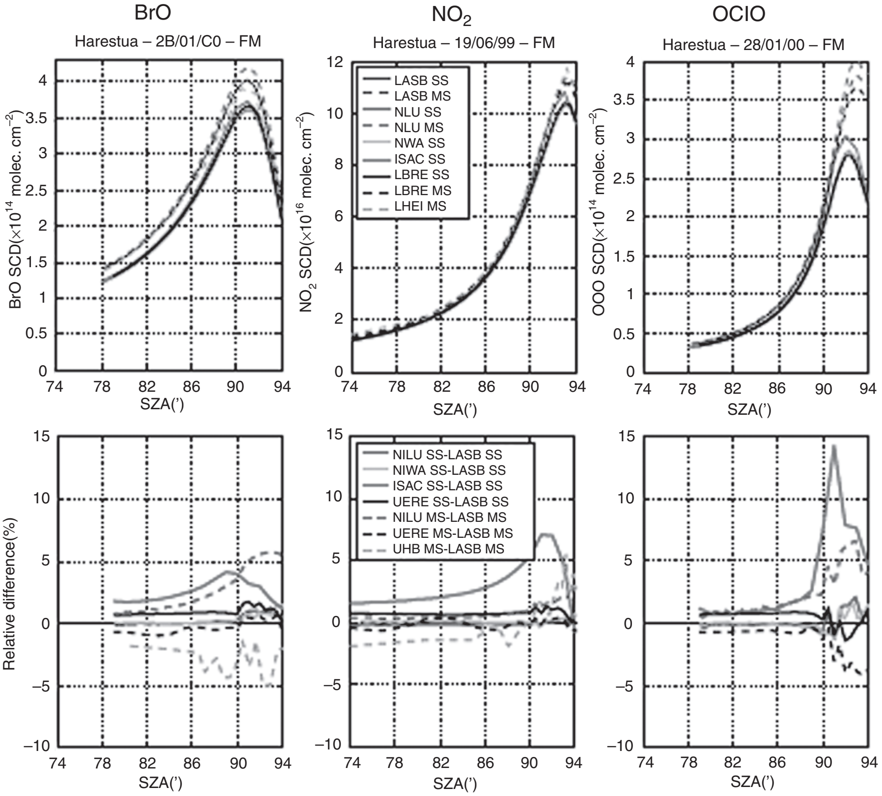

Fig. 9.15. Comparison of stratospheric and tropospheric SCDs of NO_2 at 445 nm from various RT models (from Hendrick et al., 2006)

that absorption by tropospheric species (e.g. O_4) is greatly enhanced in the off-axis viewing mode, whereas for an absorber in the stratosphere (e.g. NO_2) the absorptions for zenith and off axis geometries are comparable. One of the challenges of the 'off-axis' measurements is the increased complexity of the RT calculations. We will discuss the general implications of a non-zenith viewing geometry in the following section in more detail.

9.3.3 MAX-DOAS Measurements

The main difference between ZSL–DOAS and 'off-axis' or 'multi-axis'-DOAS is a viewing elevation angle different from 90°. This leads to an increased effective path length in the troposphere and only lesser changes in stratospheric trace gases AMF as compared to the zenith viewing geometry. Consequently, tropospheric absorbers are more heavily weighed in low elevation observations. This property is one of the main motivations to use low elevation viewing angles. However, it also increases the number of parameters that have to be considered in the RT calculations. In addition to the parameters, as we have already discussed for the ZSL case, one now also has to consider the vertical profiles of tropospheric trace gases and aerosol. The RT is also more dependent on the albedo and the solar azimuth.

The behaviour of the AMF under various conditions has been discussed by Hönninger et al. (2003) using the Monte Carlo radiative transfer model "Tracy" (v. Friedeburg, 2003), which includes multiple Rayleigh and Mie scattering, the effect of surface albedo, refraction, and full spherical geometry. To investigate the dependence of the AMF on the vertical distribution of an absorbing trace gas, Hönninger et al. (2003) considered a number of artificial profiles (Fig. 9.16). These were used together with a number of different aerosol extinction profiles and phase functions (Fig. 9.16). Calculations were performed at a wavelength of $\lambda = 352\,\mathrm{nm}$, and a standard atmospheric scenario for temperature, pressure and ozone. The vertical grid size in the horizontal was 100 m in the lowest 3 km of the atmosphere, 500 m between 3 and 5 km, and 1 km from 5 km up to the top of the model atmosphere at 70 km.

SZA Dependence of the AMF/Stratospheric AMF

The change of the AMF with SZA depends strongly on the vertical distribution of the trace gas. As in the ZSL geometry, the AMF for a stratospheric trace gas depends strongly on the SZA, in particular, at large SZA (left panel in Fig. 9.17). The dependence of tropospheric AMF is much smaller and only becomes significant above a SZA of ~75° (middle panel in Fig. 9.17). Above 75°, a small dependence on SZA can be observed. For trace gases that are

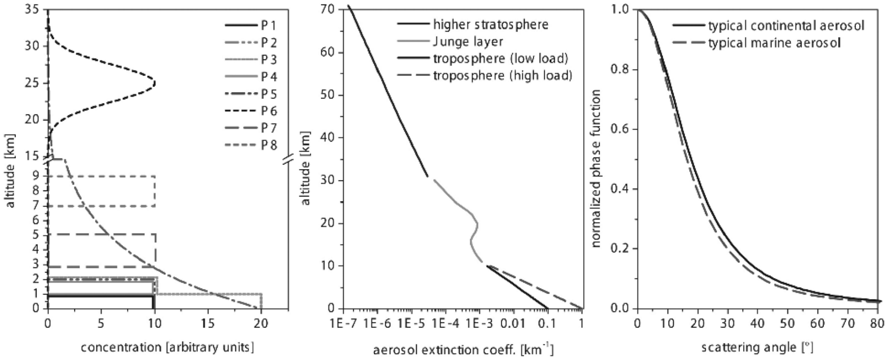

Fig. 9.16. Profile shapes of an atmospheric absorber (**left**), atmospheric aerosol (**middle**) and the aerosol scattering phase functions (**right**) used for MAX-DOAS radiation transport studies. The profiles P1–P4 assume a constant trace gas concentration in the 0–1 km and 0–2 km layers of the atmosphere. Profile P5 is that of the oxygen dimer, O_4. P5 is a purely a stratospheric profile centred at 25 km with a FWHM of 10 km (from Hönninger et al., 2003)

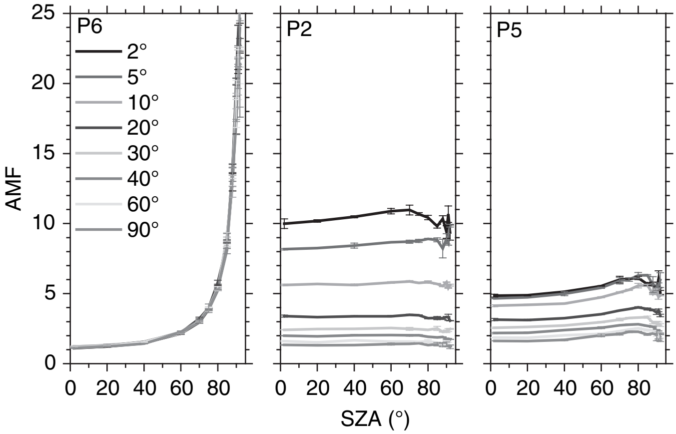

Fig. 9.17. SZA-dependence of the AMF for the typical stratospheric profile P6 and the boundary layer profile P2 as well as the O_4 profile P5 for comparison (for description of profiles see caption of Fig. 9.16). The expected strong SZA dependence is observed for the stratospheric absorber, with no significant dependence on the viewing direction. In contrast, for the tropospheric profiles P2 and P5 significant differences for the various viewing directions can be seen, while the SZA dependence is significant only at higher SZA (from v. Friedeburg, 2003; Hönninger et al., 2003)

present both in the troposphere and the stratosphere the total AMF will be a mixture of the terms.

The functional dependence of the AMF on the SZA can be best understood by analysing the altitude of the first and last scattering events between the sun and the detector (Fig. 9.18). In the model atmosphere investigated by Hönninger et al. (2003), the first scattering altitude (FSA) for $\alpha = 2°$ and SZA $< 75°$ is approximately 6 km, while the last scattering altitude, i.e. the altitude of the last scattering event before a photon reaches the MAX-DOAS instrument, is $\sim$0.6 km.

At larger SZA, the FSA slowly moves upwards in the atmosphere into the stratosphere. This is in agreement with the concept of an upward-moving most probable light path as the sun sets (see Sect. 9.1.2), and explains the SZA dependence of the stratospheric AMF. The LSA is largely independent on the SZA. Therefore, the tropospheric AMF changes little.

Dependence of AMF on Viewing Elevation

The dependence of the AMF on the viewing elevation angle, α, is strongly influenced by the vertical profile of the trace gas. Stratospheric AMFs show little dependence on α (left panel in Fig. 9.17) at low SZA because the first scattering event occurs below the stratosphere, and the light path in the stratosphere is approximately geometric, i.e. only proportional to $1/\cos(\vartheta)$. Only at larger SZA does the stratospheric AMF show a weak dependence on α.

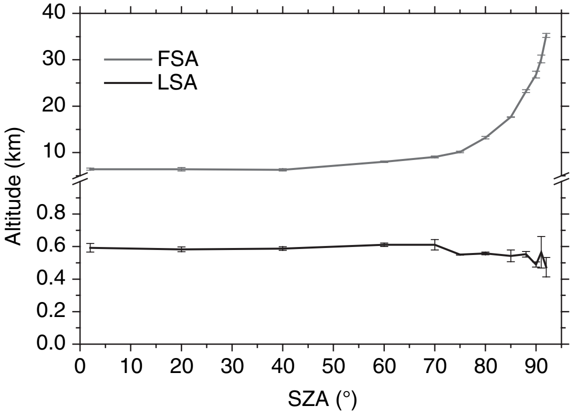

Fig. 9.18. Average altitude of first and last scattering event (FSA, LSA) for observation at 2° elevation angle. The altitude of the FSA strongly depends on the SZA, whereas the LSA altitude is largely independent of the SZA. Note the axis break at 1 km altitude and the expanded y-scale below (from Hönninger et al., 2003)

For a trace gas located in the lowest kilometre of the atmosphere, the dependence of the AMF on α is strong (middle panel in Fig. 9.17). Since most of the scattering events occur above the trace gas absorptions, the dependence is close to geometric, i.e. proportional to $1/\sin(\alpha)$ (see also Sect. 9.1.3). Deviations from this dependence may only be observed at SZA larger than 75°.

For trace gases extending above 1 km or located in the free troposphere, the dependence on α is more complicated than for the lower tropospheric case. In general, one finds that the dependence on α decreases as the altitude of the trace gas increases above the last scattering altitude. The dependence nearly disappears at the altitude of the first scattering event.

The dependence of the AMF α is the basis of MAX-DOAS. If simultaneous (or temporally close) measurements are made at different elevation angles α, there is essentially no change in ϑ and thus in the stratospheric part of the AMF. Thus, the stratospheric contribution to the total absorption can be regarded essentially a constant offset to the observed SCD.

Influence of the Trace Gas Profile Shapes

In the previous section, we indicated that the AMF depends on the vertical profile of the trace gas. Hönninger et al. (2003) calculated AMFs for six different profiles, P1–P6 in Fig. 9.19, for a pure Rayleigh scattering atmosphere, i.e. no aerosol. The dependence on the elevation angle is strongest for trace gases located close to the ground (profile P1) and decreases as the gases are located higher in the atmosphere, reaching AMFs of about 15 for very small α. A comparison with the geometric AMF shows how well $1/\sin(\alpha)$ approximates the AMF in this case. As the profiles extend further aloft

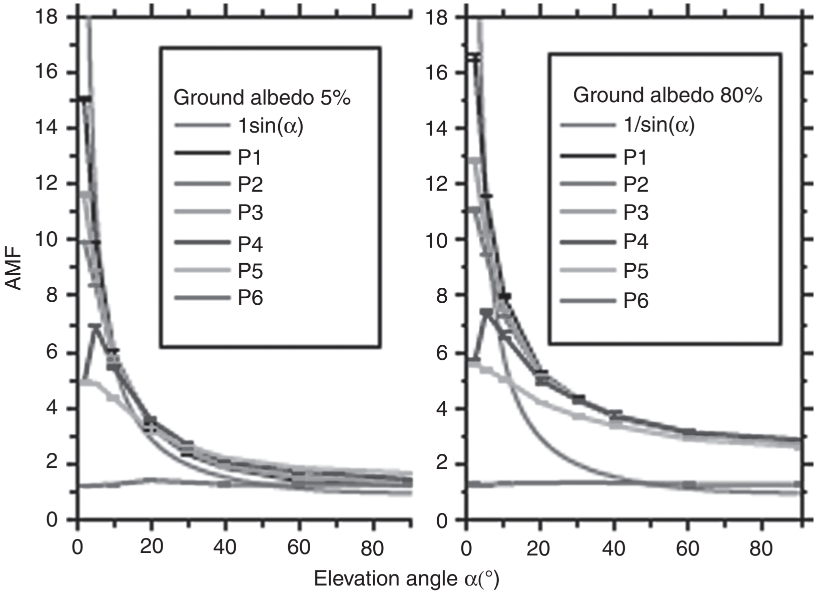

Fig. 9.19. AMF dependence on the viewing direction (elevation angle α) for the profiles P1–P6 (for description of profiles see caption of Fig. 9.16) calculated for 5% ground albedo (**left**) and 80%, albedo (**right**), respectively. A pure Rayleigh case was assumed (from v. Friedeburg, 2003; Hönninger et al., 2003)

(P2, P3, P5), the AMF decreases. Profile P5 deserves special attention since it describes the exponential decreasing concentration of atmospheric O_4. Because the O_4 levels and the vertical profile of O_4 do not change, they can be used to validate RT calculations (see Sect. 9.3.4).

For elevated trace gas layers, i.e. profile P4, the AMF peaks at $\alpha = 5$, because at lower viewing elevation angles a DOAS instrument would predominately see the air below the layer. The AMF is almost independent of the viewing direction for the stratospheric profile P6.

Dependence on Surface Albedo

Figure 9.20 shows that tropospheric AMFs (P1 – P5) are also influenced by the surface albedo. In general, higher albedos lead to larger AMF, because the reflection at the ground and the upwelling radiation will increase the effective absorption path length in the troposphere. Light that enters a DOAS instrument after being reflected at the ground may have passed parts through an absorption layer in the lower troposphere twice, thus increasing the trace gas absorption as it enters the detector. Since the effect of higher albedo increases all AMFs similarly, it has no significant effect on the elevation angle dependencies.

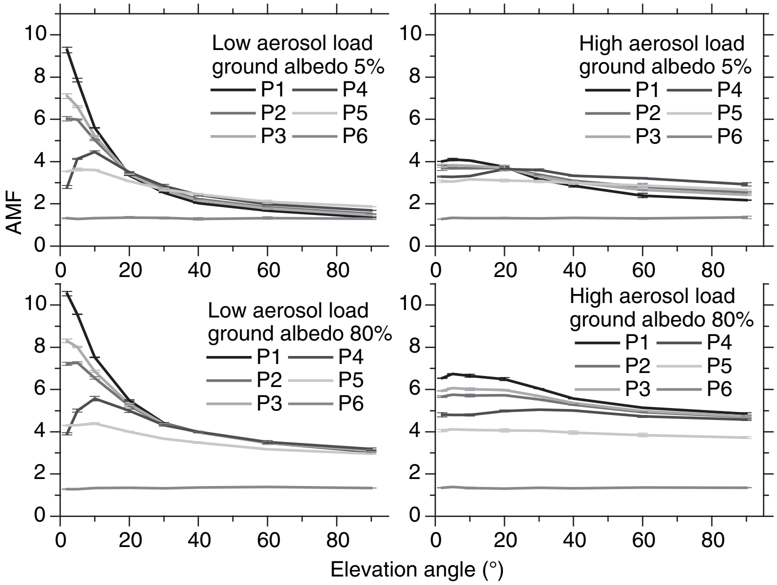

Fig. 9.20. AMF as a function of viewing direction, i.e. elevation angle α for the profiles P1–P6 (see caption of Fig. 9.16) calculated for low (**left column**) and high (**right column**) aerosol load (Fig. 9.16) and for 5% (**top**) and 80% (**bottom**) ground albedo, respectively (from v. Friedeburg, 2003)

Dependence on Aerosol Profile

The presence of aerosol particles in the atmosphere significantly enhances the scattering of radiation. Figure 9.20 illustrates how the AMFs for different viewing directions change for two different aerosol scenarios (high and low tropospheric aerosol load, Fig. 9.20) as well as for large and small surface albedo (see above). The AMF for a low aerosol load shows a similar shape to the Rayleigh case (Fig. 9.19). However, the absolute values of the AMFs at elevation angles below 20° are considerably reduced as compared to the Rayleigh case. Consequently, the geometric approximation is not good at low elevation angles, even at low aerosol loads. At high tropospheric aerosol loads, the absolute AMFs are further reduced and the dependence on α becomes much weaker.

The comparison of Rayleigh, low aerosol, and high aerosol cases also show how the dependence of the AMF on α changes with aerosol load. For trace gases in the lower part of the troposphere (P1–P3), the difference between AMF at low and high elevations slowly decreases. An extreme case of this dependence is dense fog, for which the α dependence of the AMF completely disappears. The high aerosol load and high albedo case in Fig. 9.20 also shows that in this case the AMF at very small α, i.e. 2°, can indeed be smaller than those at slightly larger α, e.g. 5°. This effect can be explained by the reduction of effective light path length at low elevation angles under these conditions (see below). The shift of the AMF maximum to larger α is even more pronounced for an elevated trace gas layer (P4), for which the maximum is at $\alpha = 5°$ for the Rayleigh case, $\alpha = 10°$ for a low aerosol load, and $\alpha = 40°$ for a high aerosol load.

The optical properties of aerosol, i.e. the scattering phase function (Fig. 9.16) and the single scattering albedo, influence the AMF little as shown by the comparison of a continental and marine aerosol in Fig. 9.21.

The fact that the tropospheric AMF decreases with increasing tropospheric aerosol load can be explained by a shorter mean free path of photons due to aerosol extinction. In particular, at low α, the light path in the lowest atmospheric layers is shorter, and a less slanted path in the higher layers is probable as illustrated in Fig. 9.22.

The last scattering altitude, which we introduced earlier, is a key parameter to understand the sensitivity of MAX-DOAS measurements towards different vertical profiles of gases and aerosol. The LSA dependence on the viewing elevation angle for different aerosol profiles is shown in Fig. 9.23. The LSA moves downward in the atmosphere as α decreases. In addition, the LSA decreases for increasing aerosol load and increasing albedo. In general, the geometric approximation for the AMF can only hold for trace gases below the LSA. Once the LSA reaches the trace gas layer, the AMF begins to decrease. Due to the α dependence of the LSA, this decrease occurs first at small α, leading to smaller AMF at very low elevation angles.

Dependence of the AMF on the Solar Azimuth Angle

In contrast to the ZSL measurements, low elevation angle measurements can show a dependence of the AMF on the SZA. In general, this dependence is

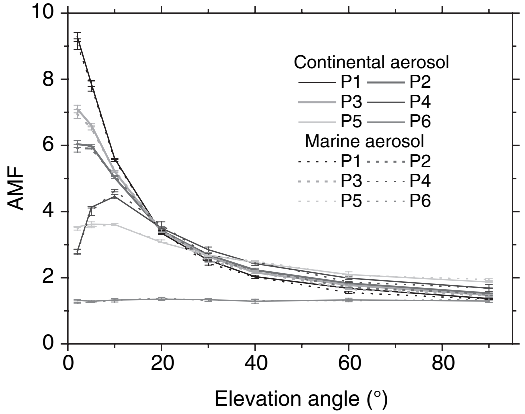

Fig. 9.21. Effect of different aerosol types on the AMF. Only small differences result from different scattering phase functions (from v. Friedeburg, 2003)

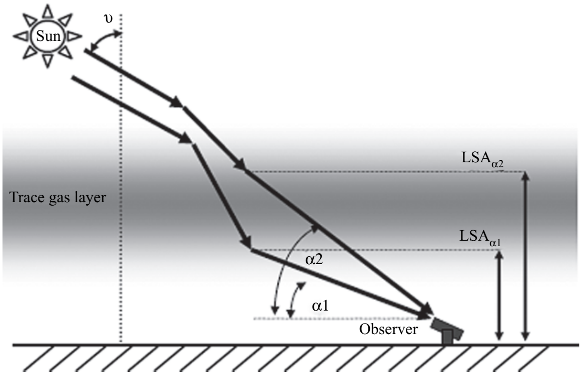

Fig. 9.22. The last scattering altitude (LSA): for low elevation angles, the mean free path in the viewing direction is shorter due to higher density and/or aerosol load. This can result in the slant path through absorbing layers at higher levels being shorter for lower elevation angles than for higher ones (from v. Friedeburg, 2003; Hönninger et al., 2003)

determined by the relative azimuth angle between the sun and the viewing direction. The effect arises due to the shape of scattering phase functions for the atmospheric scattering processes. Light paths taken by photons at different relative azimuth angles may be different, thus impacting the AMF. Figure 9.24 shows that, overall, the relative azimuth angle, here calculated for a SZA of 30° and the profile P4, has only a small influence on the AMF and

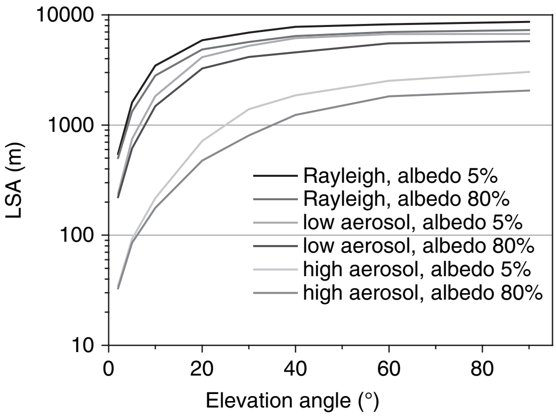

Fig. 9.23. Last scattering altitude (LSA) for pure Rayleigh, low and high aerosol load scenarios and both 5% and 80% albedo. The LSA is generally below 1 km for the lowest elevation angle and above 1 km for the highest elevation angles, especially for zenith viewing direction (from v. Friedeburg, 2003; Hönninger et al., 2003)

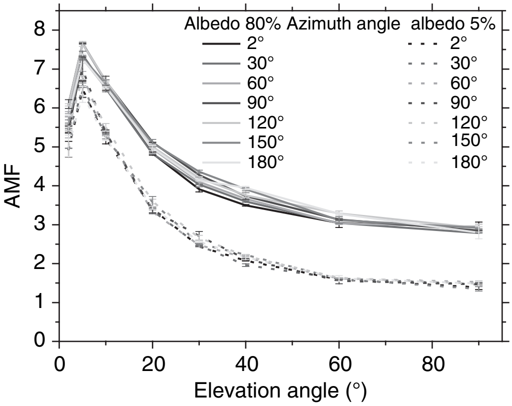

Fig. 9.24. Azimuth-dependence of the AMF for 30° SZA and profile P4 (trace gas layer at 1–2 km altitude). For relative azimuth angles between 2° (looking almost towards the sun) and 180° (looking away from the sun) only a small effect can be seen (from v. Friedeburg, 2003; Hönninger et al., 2003)

its α dependence. However, this effect is found to increase with ground albedo and tropospheric aerosol load.

9.3.4 Accuracy of MAX-DOAS AMF Calculations

Determining the accuracy of RT calculations of AMFs is a challenging task. As in the ZSL case, intercomparisons of different RT models allow the estimate of the uncertainties introduced by numerical calculations in the models. We will discuss such an intercomparison in this section. In addition, MAX-DOAS measurements of tropospheric trace gases offer another opportunity to constrain or validate RT calculations: the use of observations of stable atmospheric gases such as O_2 and O_4. This will be the topic of discussion in the second part of this section.

Model Intercomparison/Model Accuracy

The accurate calculation of AMF for low viewing elevations has only recently been implemented in RT models. Successful models include spherical geometry, refraction, and multiple-scattering. Figure 9.25 illustrates an intercomparison of four RT models, which were previously described in Sect. 9.3.1 (Hendrick et al., 2006). All models used the same boundary conditions, i.e. trace gas and aerosol profiles. Comparisons were made for viewing elevation angles of 5°, 10°, and 20°. In general, the agreement between the models was better than ±5% for the two trace gases investigated: NO_2 (Fig. 9.25) and HCHO (not shown). Hendrick et al. (2006) conclude that the largest discrepancies between the models are caused by the different treatments of aerosol scattering in each model.

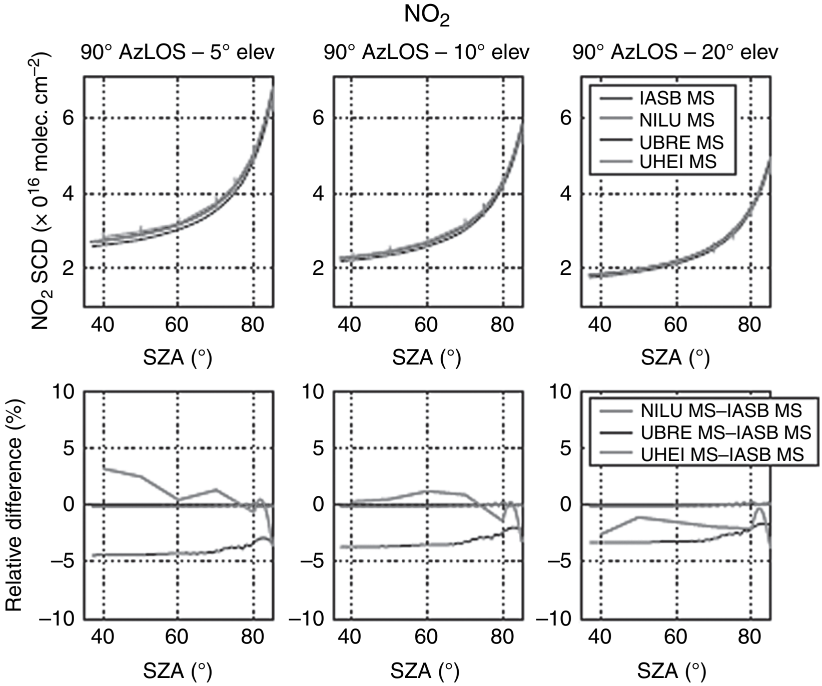

Fig. 9.25. Intercomparison of low viewing elevation slant column densities for NO_2 calculated by four different multiple scattering models (from Hendrick et al., 2006)

Validation of RT Calculations with O_2 and O_4 Measurements

One of the most challenging aspects of RT calculations is to determine the accuracies of AMFs for atmospheric measurements. The observation of the absorptions of O_2 or the oxygen dimer, O_4, offers an excellent tool to validate RT calculations and various input parameters, such as aerosol profiles, optical properties, etc. Alternatively, these measurements can be used to determine the aerosol load of the atmosphere with the goal to improving the RT calculations (Friess et al., 2006). The atmospheric O_2 and O_4 concentration profiles are well known, i.e. the O_4 profile $c_{O4}(z) = (0.21 \cdot c_{air}(Z))^2$, and are fairly constant in time (see the O_4 profile P5 in Fig. 9.16). Only small changes of the air density c_{air} on temperature and barometric pressure have to be taken into account.

The measured O_2 and/or O_4 SCDs for a series of elevation angles, e.g. from 2° to 90°, can be compared to a series of calculated O_2 and O_4 SCDs (for the temperature and pressure as recorded during the measurement). The comparison between observed and measured O_2 or O_4 SCDs can give valuable insight into the quality of the RT calculations. Furthermore, the aerosol profile can be varied until the best agreement is reached. Figure 9.26 shows

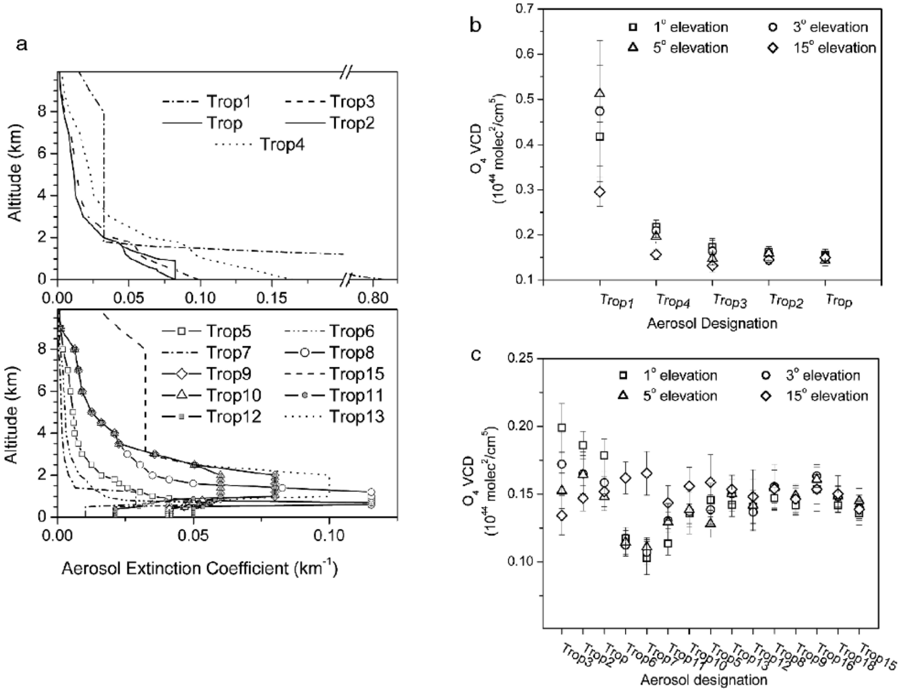

Fig. 9.26. Aerosol profile retrieval based on measurements in the polluted Marine boundary layer using observations of O_4 SCD and radiative transfer calculations based on the aerosol profiles shown in panel (**a**). The O_4 vertical column densities retrieved based on the observations and RT calculations are shown in panel (**b**) and (**c**) for two different days. The O_4 VCD with the best agreement between the four viewing elevation angles indicates the best estimate for the aerosol profile for each day (from Pikelnaya et al., 2007, Copyright by American Geophysical Union (AGU), reproduced by permission of AGU)

an example of such an optimisation for O_4 observations (Pikelnaya et al., 2007). Panels (a) in Fig. 9.26 shows different aerosol profiles that were used in a RT model to calculate AMFs of O_4. Panel (b) and (c) of Fig. 9.26 show the VCDs derived from these AMFs for O_4 SCD observation on two different days. On the first day, the profile TROP, which described a fairly constant aerosol extinction in a marine boundary layer of 700 m depth and an exponential decay above this altitude, led to the best agreement between the VCDs calculated for elevation angles of 1°, 3°, 5°, and 15°. On the second day [Panel (c) in Fig. 9.26], the profile TROP9, which consisted mainly of an aerosol layer between 1 km and 2 km altitude, led to the best agreement between the observed O_4 VCDs. This example exemplifies the sensitivity of O_4 observations on the aerosol profile and the potential of this approach to retrieve these profiles.

9.3.5 The Box-AMF Concept

With the knowledge of the aerosol profile, either through a retrieval based on O_4 slant column densities and intensities (Friess et al., 2006) or through other means, the main unknown in the MAX-DOAS RT is the vertical profile of the trace gases.

To understand the sensitivity of MAX-DOAS measurements and RT calculations on the vertical distribution, the **Box Air Mass Factor** was introduced. The Box-AMF represents the contribution of a trace gas located at a certain altitude interval, or vertical 'box', to the overall AMF under given atmospheric conditions. It is thus a measure of the sensitivity of a particular viewing direction towards an absorber being present in a specific altitude. The SCD of a trace gas, and thus indirectly the AMF, at a given elevation viewing angle, α_i, is related to the Box-AMF through the following equation:

$$S(\alpha_i) = \sum_{j=1}^{m} \left[(A_{Box})_{ij} \cdot \Delta h_j \cdot c_j \right] . \tag{9.20}$$

In this equation, Δh_j is the height of altitude interval j, c_j the concentration, and $(A_{\mathrm{Box}})_{ij}$ the Box-AMF in this interval for elevation viewing angle, α_{i}.

Figure 9.27 shows modelled Box-AMFs for trace gas layers of $\Delta h_j = 100\,\mathrm{m}$ thickness from the ground up to 2 km altitude. The Box-AMF is largest near the surface for very low elevation angles. In particular, for α smaller than 10°, the Box-AMFs vary strongly with altitude. Consequently, MAX-DOAS observations at small α are very sensitive to the shape of the vertical profile in the lower troposphere.

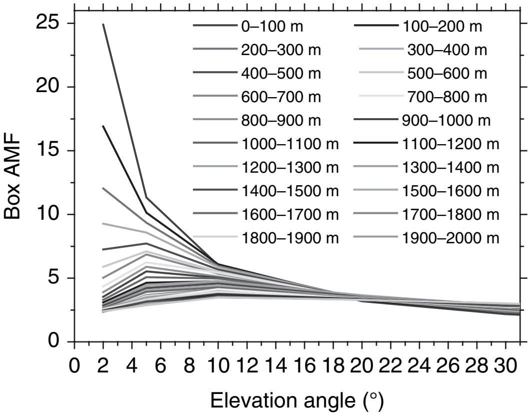

Fig. 9.27. Box AMF for the model layers below 2 km altitude. The sensitivity towards the lowest layers changes strongly for elevation angles below 10°, for elevation angles smaller than 5° the sensitivity already decreases for layers above 400 m altitude (from v. Friedeburg, 2003; Hönninger et al., 2003)

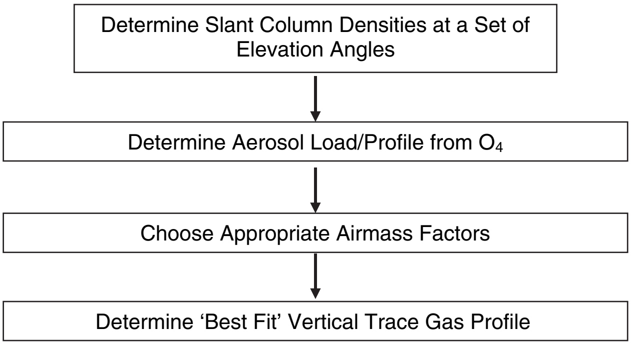

Fig. 9.28. Diagram of an AMAX-DOAS evaluation procedure including the determination of the aerosol load from O_4 observations

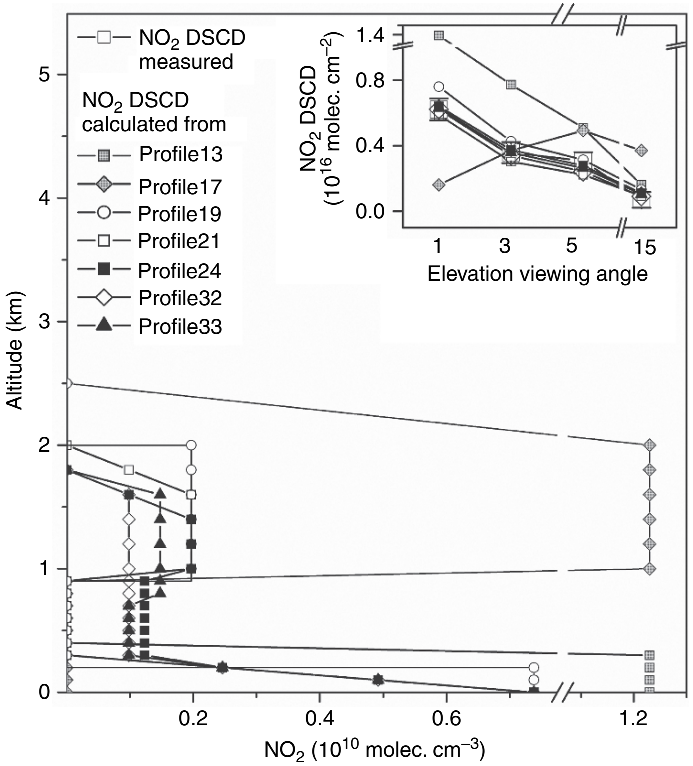

Fig. 9.29. Retrieval of the vertical profile of NO_2 in the polluted marine boundary layer of the Gulf of Maine (Pikelnaya et al., 2005). Shown are different vertical profiles of NO_2 used in the retrieval and a comparison between the calculated SCD and the observed SCD (see insert). The best agreement was found for Profile 24 (from Pikelnaya et al., 2007, Copyright by American Geophysical Union (AGU), reproduced by permission of AGU)

This sensitivity can be used to retrieve trace gas profiles from MAX-DOAS observations. By measuring trace gas SCDs at different elevation angles below 20°, one can set up a linear equation system based on (9.20), which can then be solved for the concentrations in each layer.

Figure 9.28 illustrates the steps necessary to derive trace gas profiles from MAX-DOAS measurements. The first step is measurement of O_4 and other trace gases at various viewing elevation angles, followed by the aerosol profile retrieval as shown in Fig. 9.26. In a final step, a vertical trace gas profile can be retrieved. Such a retrieval is illustrated in Fig. 9.29 for the example of a layer of NO_2 close to the ground and another layer from 1 to 2 km altitude (Pikelnaya et al., 2005). The figure shows different NO_2 profiles and a comparison between the measured and the calculated DSCDs for each profile for different viewing elevation angles. The TROP9 aerosol profile from Fig. 9.26 was used in the retrieval of the NO_2 profile for this day. The best agreement between the observed and modelled SCD was achieved for Profile 24. This example illustrates the capabilities of combined MAX-DOAS observations and RT calculations to retrieve vertical trace gas profiles.

9.4 Aircraft Observed Scattered Light (AMAX-DOAS)

Airborne platforms give high mobility to DOAS applications, allowing rapid mapping of trace gas distributions over a relatively large area. They also allow an additional degree of altitude separation by using upward and downward viewing directions (Wahner et al., 1989a,b, 1990a,b; Schiller et al., 1990; Brandjen et al., 1994; Pfeilsticker and Platt, 1994, 1997; Erle et al., 1998; McElroy et al., 1999; Petritoli et al., 2002; Melamed et al., 2003; Bruns et al., 2004).

The radiation transport for an airborne instrument will, in addition to the factors discussed earlier, depend on the flight altitude. One might expect that an upward-looking instrument will only observe trace gases located above the flight altitude. However, the RT calculations in Fig. 9.30 for viewing angles larger than 90° of an aircraft flying at 10 km altitude show that gases below the aircraft still have a considerable influence on upward-looking observations. As the viewing angle approaches the zenith, this contribution becomes smaller, but it never completely disappears. The fact that gases below the aircraft can be seen in upward-viewing direction is explained by the scattering of light originating below the flight altitude, i.e. through reflection at the ground, clouds or upward Rayleigh scattering into the detector. The contribution of this portion of the signal depends on the surface albedo, which increases this portion and the scattering properties above the aircraft, i.e. aerosol, clouds.

In downward-viewing directions and viewing directions smaller than 90°, light is observed from both above, because solar radiation first has to cross this region, and below the aircraft (Fig. 9.30). The decrease of the weighing functions towards the ground in Fig. 9.30 is caused by the decreasing intensity

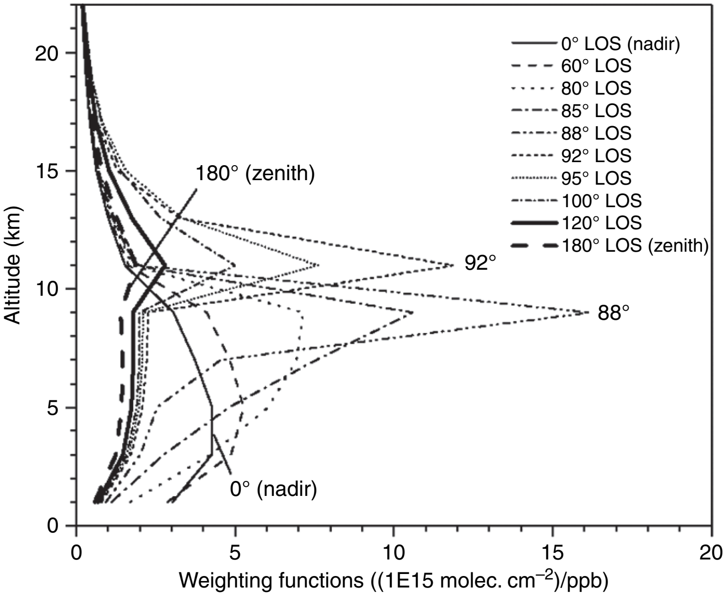

Fig. 9.30. Calculated weighting functions (Box AMFs) for a flight altitude of 10 km and NO_2 profiles anticipated for mid latitudes on the northern hemisphere spring at 51.6°SZA. Each weighting function corresponds to a different line of sight (LOS). Nadir direction is 0°. The magnitude of the weighting functions is small at the surface and above 15 km, revealing that the slant columns are not very sensitive to NO_2 in these regions (from Bruns et al., 2004)

scattered into the detector at lower altitudes due to higher extinction near the ground. The weighing functions in the downward-viewing direction strongly depend on surface albedo and wavelength.

It should be noted here that the presence of clouds below or above the aircraft considerably complicate the RT calculations and the interpretation of airborne DOAS observations.

9.5 Satellite Observed Scattered Light

Atmospheric trace gases can also be observed by DOAS from satellite platforms by measuring the light backscattered from the atmosphere and the surface. Several viewing geometries are possible. The most popular viewing geometries are Nadir View and Limb View. Many aspects of the RT for satellite observations are similar to those for the ground-based and aircraft-based observations discussed earlier. This section will thus concentrate on the particular problems arising in spaceborne observations.

9.5.1 Radiative Transfer in Nadir Geometry – the Role of Clouds

In near-nadir geometry (see Fig. 9.31), the instrument looks down to a point on earth below its current position. The radiation observed by the satellite instrument originates as solar light, which is backscattered or (diffuse) reflected from the atmosphere and the earth's surface, respectively.

The AMF for the case of pure backscattering from the earth's surface (Fig. 9.31a) can be approximated by geometric considerations. Neglecting the curvature of the earth, the AMF for an SZA ϑ and the observation angle (angle between nadir and actual observation direction), α, is given by:

$$A_{\text{surface}} = 1/\cos\vartheta + 1/\cos\alpha\ .$$

Since the radiation passes the atmosphere twice, A_{surface} is always greater than 2 (see Fig. 9.32).

In reality, however, a fraction of the radiation will be backscattered in the atmosphere (Fig. 9.31b). Figure 9.32 shows a comparison between the geometric AMFs and those calculated with a RT model for a stratospheric and tropospheric absorber. The relative ratio of surface and atmosphere backscattered radiation depends on various factors. The contribution of Rayleigh scattering increases towards shorter wavelengths. Consequently, the contribution of the lower atmosphere decreases for lower wavelength, and satellite observations in the UV are not very sensitive to trace gases in the atmospheric boundary layer. Similarly, trace gas absorptions, in particular those of ozone, can change the contribution of the lower atmosphere. Below 300 nm, where the ozone layer absorbs most radiation, the troposphere cannot be observed. On the other hand, this wavelength dependence can be used for vertical trace gas

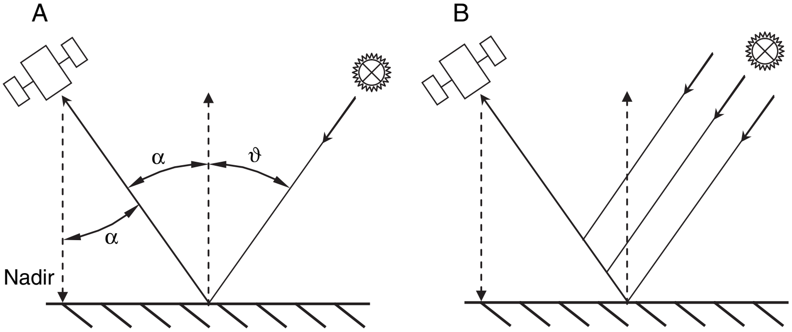

Fig. 9.31. Geometry of a (near) nadir viewing satellite instrument and a sketch of the associated radiation transport in the atmosphere: (**a**) Without scattering in the atmosphere the instrument would only record radiation scattered back from the surface, the AMF would always exceed 2. (**b**) In reality, in addition to reflection from the surface, as in the case of other Scattered-Light DOAS geometries, there is an infinite number of possible paths of scattered radiation between the light source (i.e. the sun) and the instrument

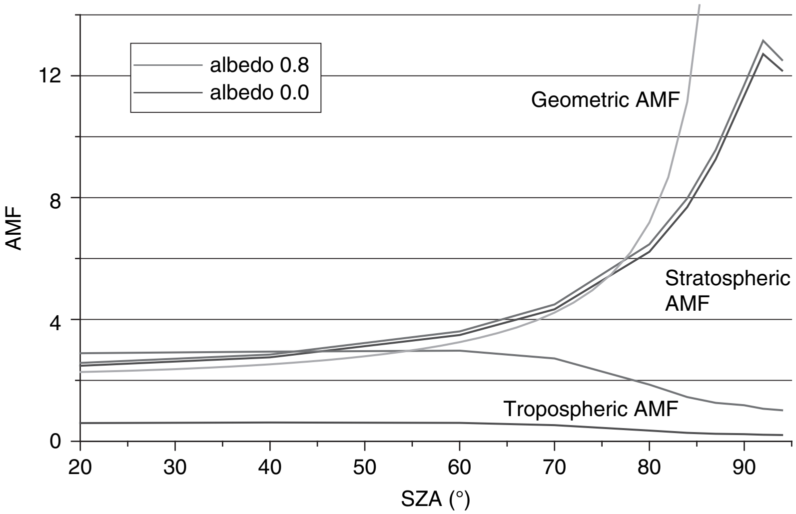

Fig. 9.32. Airmass factors for a nadir viewing satellite instrument as a function of solar zenith angle ϑ for two ground albedo values. Three cases are shown: Geometric AMF ($1/\cos\vartheta$), AMF for a tropospheric trace gas profile, AMF for a stratospheric trace gas profile

profiling if a gas is measured at different wavelengths. Mie scattering in the atmosphere will enhance the fraction of backscattered light above an aerosol layer while decreasing the contribution of the trace gases below the layer. An extreme example is clouds that basically block the contribution of the atmosphere to the SCD below the cloud. However, tropospheric aerosol can also considerably change the weighing of different altitudes in the atmosphere in satellite observations. Backscatter and absorption in the atmosphere will generally reduce the AMF to values below A_{surface} for a given set of angles ϑ and α (Fig. 9.32). The surface albedo will predominantly impact the tropospheric AMF (Fig. 9.32). Higher albedos lead to considerably higher AMF.

Another important consequence of part of the radiation being scattered in the atmosphere rather than traversing it entirely is a reduction in sensitivity towards lower altitudes. Thus, a trace gas layer located close to the surface will give a lower apparent column density than a layer of the same VCD higher up in the atmosphere. This is illustrated in Fig. 9.33 showing the Box AMFs or sensitivity as a function of altitude for high and low albedo at UV and visible wavelengths.

Another RT problem, particular to satellite observations, arises from the spatial averaging of satellite observations. Typically, a satellite observes an area of the earth surface in the range of 100–1000 km^2. The large extent of this ground pixel leads to an averaging of parameters such as the surface albedo. A particular problem in this context is the possibility of partially cloudy ground pixels. Clouds will mask the fraction of the total trace gas column

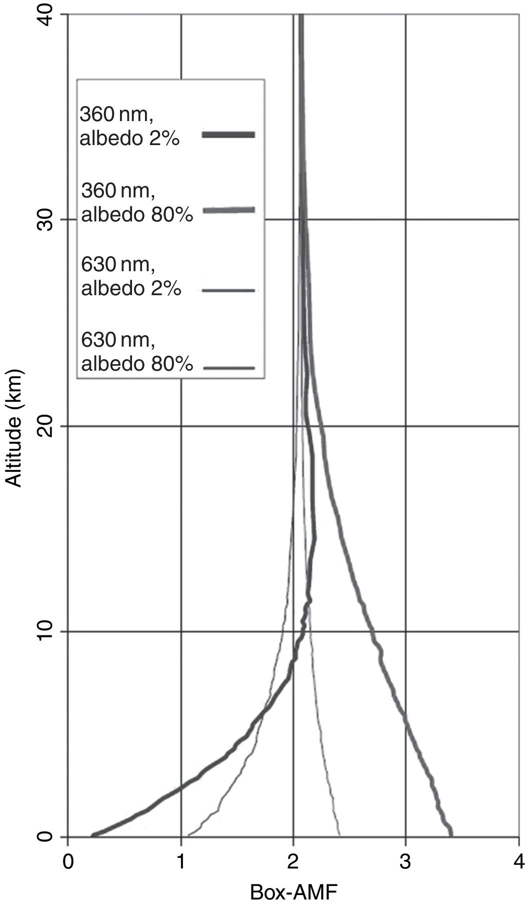

Fig. 9.33. Box airmass factors for a nadir viewing satellite – instrument as a function of box (trace gas layer) altitude for 360 nm and 630 nm and for two ground albedo values (2% and 80%), respectively (Figure courtesy of T. Wagner)

below the cloud. The total intensity received by the satellite instrument (neglecting radiation reflected from the surface below the cloud) is given by:

$$I_S = I_0 \cdot (f \cdot B_{\text{Cloud}} + (1 - f) \cdot B_{\text{Surface}}) \ ,$$

where B_{Cloud} and B_{Surface} denote the albedo of cloud and surface, respectively, and f is the fraction of the pixel covered by the cloud. Unfortunately, the effect of clouds is larger than expected at the first glance: For instance, assuming $B_{\text{Cloud}} = 0.8$, $B_{\text{Surface}} = 0.05$ and $f = 0.5$, only about 6% of the signal comes from the cloud-free part of the pixel. Accordingly, the derived column density will be dominated from the cloud-covered part of the pixel. In reality, the situation will be somewhat better, since some of the light penetrating the cloud towards the surface will actually return through the cloud to the instrument. Also, correction of the cloud effect is possible, but requires a very precise determination of the cloud fraction f.

In view of the importance of cloud correction for the analysis of tropospheric trace gases, an accurate and reliable cloud detection algorithm is essential for the correct determination of tropospheric trace gas column densities. While detection of clouds from satellite, e.g. through thermal IR radiometry, has been in use for a long time, it turns out that DOAS-type satellite instruments are better served by cloud detection using the same instrument's data.

A series of algorithms were developed for the retrieval of cloud parameters. For instance, for the Global Ozone Monitoring Experiment (GOME), there is the official GOME cloud product' ICFA (Initial Cloud Fitting Algorithm) (Kuze and Chance, 1994) and the FRESCO algorithm (Fast REtrieval Scheme for Clouds from the Oxygen-A-Band) (Koelemeijer et al., 2001), both using the GOME channels with moderate spectral resolution. In addition, there are several algorithms using broad radiometers of GOME with higher spatial resolution, the Polarization Monitoring devices (PMD).

Two different quantities are usually applied for cloud retrieval: (1) The absorption of the O_2-A-Band. Clouds reduce the penetration of light down to low layers of the atmosphere, thus the retrieved O_2 column density is reduced for a cloudy pixel as compared to a cloud-free measurement, where the absorption mainly depends on cloud coverage, cloud albedo, and cloud top height. This approach is used by ICFA and FRESCO, but cannot be applied to the PMD instruments because of their insufficient spectral resolution. (2) The main idea of a second class of algorithms is that clouds can also be identified through the overall intensity of reflected light, which is hardly affected by trace

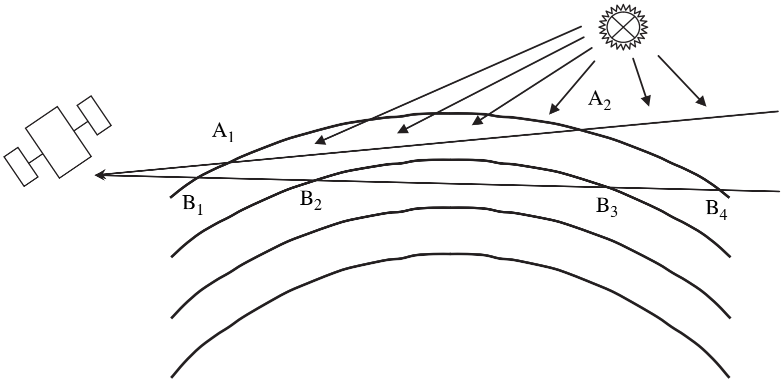

Fig. 9.34. Geometry of a limb viewing satellite instrument and a sketch of the associated radiation transport in the atmosphere. As in the case of other Scattered-light DOAS geometries there are an infinite number of possible light paths between the light source (i.e. the sun) and the instrument

gas absorptions, because clouds are usually brighter than the surface. These intensities are mainly independent of cloud top height, but they also depend on cloud coverage and cloud albedo. This approach is applied using small spectral windows of the detectors with moderate spectral resolution (FRESCO) and by the algorithms using the PMD instruments. All these algorithms retrieve an effective cloud fraction, a parameter that combines cloud coverage (cloud abundance) of the pixel and cloud albedo (Grzegorski et al., 2006).

9.5.2 The Analysis of Satellite-limb Scattered Light Observations

In limb-view geometry, the radiation scattered from the edge of the earth's disk (the limb) is observed by a suitable telescope. This mode of observation allows the derivation of vertical trace gas concentration profiles at relatively high accuracy and vertical resolution. The RT in this case is dominated by the scattering events at different altitudes within the atmosphere. Synthetic limb measurements and weighting functions (WFs) with several orders of scattering and surface reflection were computed by Kaiser and Burrows (2003). Comparisons reveal the wavelength-dependent contributions of single scattering and the second orders of scattering and surface reflection, showing that the single-scattering approximation is sufficient for the calculation of the weighing functions during the retrieval process. Models such as those described for the MAX-DOAS evaluations are thus also usable for the AMF calculation for LIMB geometry.